International Journal of Solids and Structures 49 (2012) 2359–2372

Contents lists available at SciVerse ScienceDirect

International Journal of Solids and Structures

journal homepage: www.elsevier.com/locate/ijsolstr

Guided waves dispersion analysis for prestressed viscoelastic waveguides by means of the SAFE method

M. Mazzotti [a], A. Marzani [a,*], I. Bartoli [b], E. Viola [a]

[a] Dipartimento di Ingegneria Civile, Ambientale e dei Materiali (DICAM), Università degli Studi di Bologna, Viale Risorgimento 2, 40136 Bologna, Italy
[b] Civil, Architectural & Environmental Engineering Department, Drexel University, 3141 Chestnut St., Philadelphia, PA 19104, USA

ARTICLE INFO

Article history:
Received 12 January 2012
Received in revised form 5 April 2012
Available online 23 May 2012

Keywords:
Stress guided waves
Prestress
Viscoelasticity
Dispersion
Semi-Analytical Finite Element
Energy velocity
Nonconservative forces

ABSTRACT

The work focuses on the effect of a general state of initial stress on the dispersion behavior of guided waves in viscoelastic waveguides. To this purpose, an extension of the Semi Analytical Finite Element (SAFE) method is proposed to formulate the wave equation and to extract the waves modal properties in viscoelastic prestressed waveguides. The wave equation is derived in linearized incremental form within an updated Lagrangian framework, where the prestressed configuration is considered to be slightly deviated from the corresponding unstressed one. Next, by using the SAFE method and the Boltzmann superposition principle, a linear algebraic system of equations is obtained in the complex wavenumber-frequency domain. Dispersive guided waves wavelengths, phase velocity, group velocity and attenuation, are extracted by solving a polynomial eigenvalue problem. A modal formula for the wave energy velocity calculation, that exploits the wave equation SAFE matrices only, is proposed. Such formula is based on the linearized incremental form of the Poynting theorem obtained by manipulating the energy balance principle expressed in material description.

Numerical examples on a hysteretic 113A standard rail profile and on an ASME 1-1/2 Schedule 160 steel pipe, considering various states of initial stress and applied loadings, are presented to show the effect of prestress on the dispersive properties of mechanical waves in viscoelastic waveguides.

1. Introduction

The importance of ultrasonic guided waves in the field of nondestructive testing and structural health monitoring has increased considerably in recent years. Guided waves are used for damage detection, damage localization and material characterization. Lately, researchers are also trying to use guided waves for revealing the state of prestress in waveguides. All these applications require an accurate knowledge of the dispersive characteristics of guided waves (i.e. the solutions of the guided wave equation must be known at several frequencies).

For the case of waves propagation in solids with a predeformation or a prestress state, a first rigorous mathematical treatment of the problem can be found in the works by Biot (1940, 1957, 1965) and Hayes (1963). Through the years, the problem has been subjected to an intensive research. Williams and Malvern (1969) used the harmonic analysis to get the phase-velocity dispersion curves for prestressed circular rods, flat plates and unbounded mediums considering both strain-rate-independent and strain-rate-dependent constitutive equations. The effect of tensile and compressive axial loads on the dispersive characteristic of elastic waves propagating in submerged beams was investigated by Cook and Holmes (1981). More recently, Bhaskar (2003) studied the dispersion relations for propagative and evanescent modes with bending-torsion coupling, while Tanuma and Man (2006) considered Rayleigh waves propagating along the free surface of a prestressed anisotropic media, deriving a first-order perturbation formula for the phase velocity shift of Rayleigh waves from its comparative isotropic value. Frikha et al. (2011) have demonstrated that the effect of a compressive or tensile axial load on the elastic wave propagation in helical beams is significant for the four propagating modes in a low-frequency range.

The wave propagation problem in waveguide-like structures has been investigated in the literature using different mathematical approaches. Osetrov et al. (2000) applied the Transfer Matrix Method (TMM) to study Surface Acoustic Waves (SAW) propagating in anisotropic and hyperelastic layered systems under residual stress, including also changes in density, modification of the elastic stiffness tensor by residual strain and third-order stiffness constants. Lematre et al. (2006) applied matrix methods to predict Lamb, Shear Horizontal (SH) and SAW propagation in piezoelectric plates subjected to different stress profiles and to calculate the acoustoelastic effect on Lamb wave propagation in stressed thin-films as well as in multilayered heterostructures under biaxial

* Corresponding author. Tel.: +39 0512093504; fax: +39 0512093496.
E-mail address: alessandro.marzani@unibo.it (A. Marzani).
URL: http://alessandromarzani.people.ing.unibo.it (A. Marzani).

0020-7683/$ - see front matter © 2012 Elsevier Ltd. All rights reserved.
http://dx.doi.org/10.1016/j.ijsolstr.2012.04.041

residual stresses. In their work, Chen and Wilcox (2007) proposed a three-dimensional finite element based procedure to predict the effect of axial load on the dispersive properties of guided waves in elastic waveguides of arbitrary cross section such as rods, plates and rails, validating the method at low frequencies by using analytical formulae for low order theories.

The prediction of dispersive characteristics of waves traveling along waveguides of arbitrary cross section represents a computationally expensive problem, especially when dispersive data is required at high frequencies. For waveguides of arbitrary but constant cross section the Semi Analytical Finite Element (SAFE) technique represents a very efficient tool, since it allows to discretize the waveguide cross section only, reducing drastically the dimension of the problem (Bartoli et al., 2006; Treyssède, 2008; Mu and Rose, 2008).

To date, Semi Analytical Finite Element (SAFE) formulations were predominantly exploited for axially-loaded waveguides of linear elastic materials only (Loveday, 2009). In his work, Loveday included the effect of the axial load, resulting in a additional geometric stiffness matrix proportional to the mass matrix through the ratio between the axial stress and mass density. At low frequencies numerical results were shown to be in good agreement with those predicted by the Euler–Bernoulli beam theory. This extension has been used subsequently to evaluate the influence of axial load changes in rails by using sensitivity analysis and phase shift (Loveday and Wilcox, 2010) as well to support the development of a prototype aimed at predicting incipient buckling in Continuously Welded Rails (CWR) (Bartoli et al., 2010).

Experimental validations of the various formulations proposed in the literature can be found in different works. For instance, in their work, Chaki and Bourse, 2009 applied simplified acoustoelastic formulations to calibrate a guided ultrasonic wave procedure for monitoring the stress level in seven-wire steel strands while Shen et al. (2008) used guided waves to localize defects in pipes bearing high pressure gases.

Since the use of guided waves for long range inspection applications is increasing, a further development of the SAFE formulation is necessary to extend it beyond the case of mono-axial prestress states. To this aim, the present study generalizes the SAFE formulations to viscoelastic waveguides subject to a three-dimensional state of prestress.

The present extension allows thus to predict the effect of prestress on the guided waves group and energy velocity as well as the wave attenuation. In this context, Caviglia and Morro (1998, 1992) provided a rigorous mathematical treatment of the energy flux and dissipation of waves traveling in prestressed anisotropic viscoelastic solids.

In their work, Degtyar and Rokhlin (1998) used an energy velocity formula to investigate the reflection/refraction problem for elastic wave propagation through a plane interface between two anisotropic stressed solids and between a fluid and a stressed anisotropic solid with arbitrary propagation directions and arbitrary incident wave type.

The present paper is organized in the following manner: in Section 2, the equilibrium equations of the incremental linearized theory are reviewed including the general state of prestress, the viscoelastic properties of the material and the effect of nonconservative forces. In Section 3 the discretized system governing the wave propagation problem is derived via the application of the SAFE method. The group velocity proposed first in Loveday (2009) is then updated to account for the new stiffness operators without including the viscoelastic effect, which is taken into account in the energy velocity formula derived from the energy balance principle recasted in incremental form. The scheme developed is sufficiently general to cover also prestressed waveguides of viscoelastic anisotropic materials. The formulation can be relevant in the design of several long range non-destructive techniques based on guided waves. In particular, it can be extremely helpful in the prediction of testing results for ultrasonic guided wave based screening of roller straightened rails (Schleinzer and Fischer, 2001; Keller et al., 2003; Biempica et al., 2009; Ringsberg and Lindbäck, 2003), where the stress state has to be limited to prevent crack propagations and rail failures, as well as in pressurized pipelines carrying gases, where the distance of propagation of guided waves is of primary importance (Shen et al., 2008; Shin and Rose, 1999). The last two applications are considered in Section 4, where the changes in the dispersive behaviors due to prestress are shown.

2. Wave equation in incremental form

The incremental equations of motion are derived in the Lagrangian framework depicted in Fig. 1, where $\mathcal{C}^0$ is the stress-free initial configuration, $\mathcal{C}$ denotes the prestressed configuration while $\mathcal{C}'$ is the current configuration in which the prestressed waveguide deforms due to wave motion. The general particle at $\mathbf{x}$ in the prestressed configuration is subjected to a stress field denoted by the Cauchy stress tensor $\mathbb{T}^0(\mathbf{x})$, which is assumed to satisfy the static equilibrium conditions with the external applied body and surface forces, $\mathbf{f}^0$ and $\mathbf{t}^0$, respectively.

Although the Total Lagrangian (TL) description is widely used in the context of nonlinear solid mechanics, here the Updated Lagrangian (UL) formulation results convenient since the initial static displacement field $\mathbf{u}^0$ can be accounted implicitly in the finite element mesh. The TL description obviously still remains of general validity but the nonlinear strain–displacement relations include additional high-order terms in $\mathbf{u}^0$ (Bathe, 1996), leading to more complicated equations.

However, when deformations are superimposed on finite strains, the prestressed state is generally assumed identical or at most slightly deviated from the unstressed state and the TL and UL formulations confused by posing $\mathbf{x}^0 \approx \mathbf{x}$. This simplification cannot be applied when large strains and stresses are involved since it requires the use of appropriate incremental kinematic and constitutive relations (Yang and Kuo, 1994; Bathe, 1996; Bažant and Cedolin, 1991). Such cases are not considered here but are of great importance, especially when the stress level reaches the same order of magnitude of the incremental tangential moduli or, if the body is not thin, when the incremental material moduli shows high anisotropy (Bažant and Cedolin, 1991).

According to the UL description, the $\mathcal{C}$ configuration is taken as reference and it is computed from $\mathcal{C}^0$ considering the initial static displacement $\mathbf{u}_0$, which is assumed to be known, for example, from previous static analysis. The current configuration vector $\mathbf{x}'(\mathbf{u}) = \mathbf{x} + \mathbf{u}$ at time t results from the superimposition of a small incremental time-dependent displacement field $\mathbf{u} = [u_x,\ u_y,\ u_z]^{\mathrm{T}}$ due to the mechanical waves on the prestressed configuration $\mathbf{x}$. For the sake of convenience in the rest of this work the subscript indexes referring to the x, y and z directions are freely interchanged with the subscripts 1, 2 and 3, respectively.

2.1. Incremental strain–displacement relations

The geometric nonlinearities associated with the initial stress enter the problem via the kinematic relations, in force of the finite strains assumption. For conciseness, with the term "finite" the differences in magnitude of strains between the prestress field and the one associated with the ultrasonic excitations, which is much smaller, is indicated.

For instance, in many practical applications waveguides can be treated as slender structures for which magnitudes of strains arising during their service state are generally included in the range of $10^{-4} \div 10^{-3}$, while typically guided waves generate strains in the

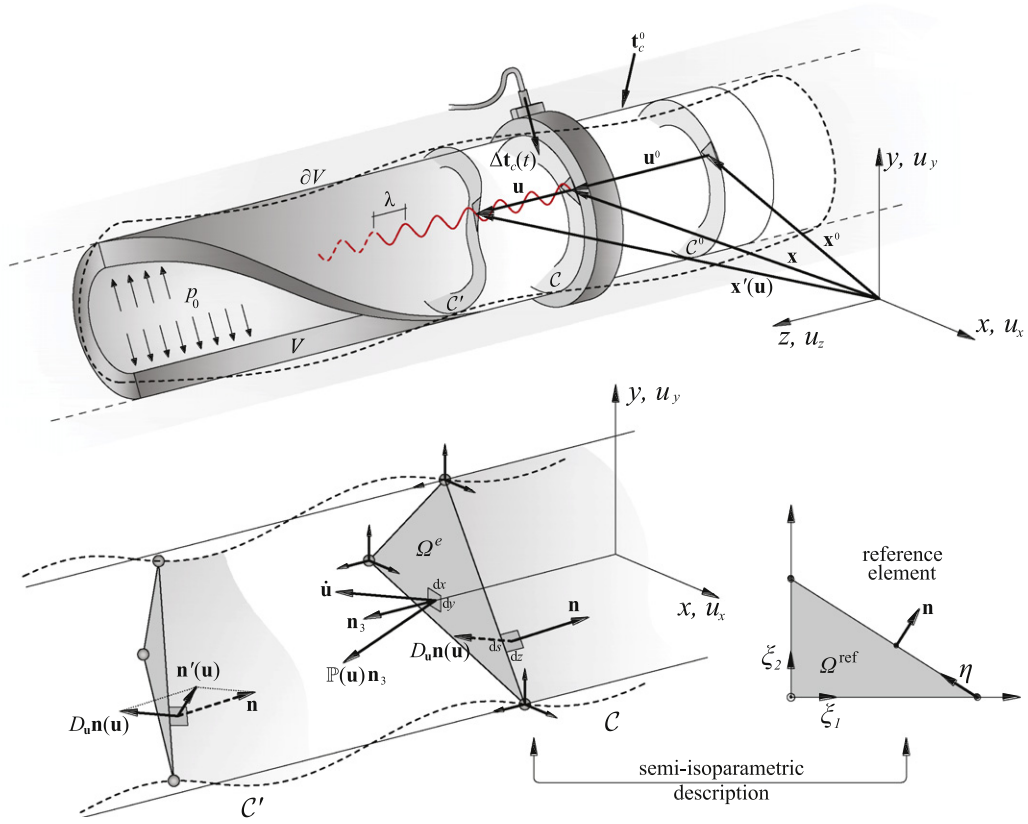

Fig. 1. Fundamental configurations for the wave propagation problem in prestressed waveguides.

order of 10^{-7} (Rose, 2004; Man, 1998). This means that typical strains involved in slender structures can be considered "finite" if compared with ultrasonic strains even if the prestressed configuration posses an elastic reserve.

In this context the appropriate strain measure is represented by the Green–Lagrange (GL) strain tensor $\mathbf{E}(\mathbf{u}) = \frac{1}{2}\left[\nabla\mathbf{u} + (\nabla\mathbf{u})^{\mathrm{T}} + (\nabla\mathbf{u})^{\mathrm{T}}\nabla\mathbf{u}\right]$, whose symmetric components can be collected in the 6×1 vector $\boldsymbol{\epsilon}(\mathbf{u}) = \boldsymbol{\epsilon}_L(\mathbf{u}) + \boldsymbol{\epsilon}_{NL}(\mathbf{u})$, where

$$\boldsymbol{\epsilon}_L(\mathbf{u}) = \left[\mathcal{L}_x\frac{\partial}{\partial x} + \mathcal{L}_y\frac{\partial}{\partial y} + \mathcal{L}_z\frac{\partial}{\partial z}\right]\mathbf{u} \tag{1}$$

$$\boldsymbol{\epsilon}_{NL}(\mathbf{u}) = \frac{1}{2}\left[\frac{\partial\mathbf{u}^{\mathrm{T}}}{\partial x}\frac{\partial\mathbf{u}}{\partial x}, \frac{\partial\mathbf{u}^{\mathrm{T}}}{\partial y}\frac{\partial\mathbf{u}}{\partial y}, \frac{\partial\mathbf{u}^{\mathrm{T}}}{\partial z}\frac{\partial\mathbf{u}}{\partial z}, 2\frac{\partial\mathbf{u}^{\mathrm{T}}}{\partial y}\frac{\partial\mathbf{u}}{\partial z}, 2\frac{\partial\mathbf{u}^{\mathrm{T}}}{\partial x}\frac{\partial\mathbf{u}}{\partial z}, 2\frac{\partial\mathbf{u}^{\mathrm{T}}}{\partial x}\frac{\partial\mathbf{u}}{\partial y}\right]^{\mathrm{T}} \tag{2}$$

are the vectors of linear and nonlinear strain components, respectively. In Eq. (1) the compatibility operators $\mathcal{L}_i$ are defined as

$$\mathcal{L}_x = \begin{bmatrix}1&0&0\\0&0&0\\0&0&0\\0&0&0\\0&0&1\\0&1&0\end{bmatrix},\quad \mathcal{L}_y = \begin{bmatrix}0&0&0\\0&1&0\\0&0&0\\0&0&1\\0&0&0\\1&0&0\end{bmatrix},\quad \mathcal{L}_z = \begin{bmatrix}0&0&0\\0&0&0\\0&0&1\\0&1&0\\1&0&0\\0&0&0\end{bmatrix}. \tag{3}$$

Assuming as incremental those quantities associated with the difference of motion between the $\mathcal{C}'$ and $\mathcal{C}$ configurations, the linearized incremental strain–displacement relations are obtained for small increments $\mathbf{u}(\mathbf{x},t)$ by means of a first order Taylor series expansion $f(\mathbf{x}+\varepsilon\mathbf{u}) - f(\mathbf{x}) = D_\mathbf{u}f(\mathbf{x})$ in the neighborhood of the prestressed configuration, where $D_\mathbf{u}f(\mathbf{x}) = \frac{\mathrm{d}}{\mathrm{d}\varepsilon}\big|_{\varepsilon=0} f(\mathbf{x}+\varepsilon\mathbf{u})$ denotes the directional derivative at $\mathbf{x}$ in the direction of the incremental displacement $\mathbf{u}$. Accordingly, the linearization of the GL strain tensor and the virtual GL strain tensor take the form $D_\mathbf{u}\boldsymbol{\epsilon}(\mathbf{u}) = \boldsymbol{\epsilon}_L(\mathbf{u})$ and $D_\mathbf{u}\delta\boldsymbol{\epsilon}(\mathbf{u}) = \delta\boldsymbol{\epsilon}_{NL}(\mathbf{u})$ respectively, where δ denotes the first variation with respect to $\mathbf{u}$.

2.2. Linearized stress–strain relations

The increment of stress related to any strain increment $\boldsymbol{\epsilon}(\mathbf{u})$ results to be small as it depends on the small amplitude waves assumption. From an energetic point of view, the use of the 2nd Piola–Kirchhoff stress tensor $\mathbb{S}(\mathbf{u})$ is required as work-conjugate of the GL strain tensor. Because of only small amplitude waves are applied on the initial prestressed configuration, the state of stress in the current configuration will differ slightly from the prestressed state. Therefore, the symmetric part of the incremental 2nd Piola–Kirchhoff stress tensor, $\mathbf{s}(\mathbf{u}) = [S_{xx},\ S_{yy},\ S_{zz},\ S_{yz},\ S_{xz},\ S_{xy}]^{\mathrm{T}}$, can be linearized as

$$D_\mathbf{u}\mathbf{s}(\mathbf{u}) = \frac{\partial\mathbf{s}(\mathbf{u})}{\partial\boldsymbol{\epsilon}(\mathbf{u})}\bigg|_{\mathbf{u}=0} D_\mathbf{u}\boldsymbol{\epsilon}(\mathbf{u}) = \mathbb{D}^0(\mathbf{x})\boldsymbol{\epsilon}_L(\mathbf{u}) \tag{4}$$

where $\mathbb{D}^0_{ij}(\mathbf{x}) = \partial\mathbf{s}_i(\mathbf{u})/\partial\boldsymbol{\epsilon}_j(\mathbf{u})\big|_{\mathbf{x}'=\mathbf{x}}$ is the 6×6 fourth order symmetric tensor of tangential moduli expressed in Voigt notation $(i,j = 1,2,\ldots,6)$ and referred to the prestressed configuration.

If an isotropic material with linear viscoelastic behavior is considered, the Boltzmann superposition principle can be used to express the incremental stress in force of the small amplitude waves, and the linearized incremental 2nd Piola Kirchhoff stress tensor in Eq. (4) can be rewritten in terms of convolution integral as (Lee and Oh, 2005; Christensen, 2010)

$$D_\mathbf{u}\mathbf{s}(\mathbf{u}) = \int_{-\infty}^{t} \mathbb{D}^0(\mathbf{x}, t-\tau)\frac{\partial\boldsymbol{\epsilon}_L(\mathbf{u}(\mathbf{x},\tau))}{\partial\tau}\,\mathrm{d}\tau \tag{5}$$

being now $\mathbb{D}^0(\mathbf{x}, t-\tau)$ the fourth order symmetric tensor of relaxation functions and t the current time instant.

2.3. Linearized incremental equilibrium equations

The equilibrium in incremental form is obtained by subtracting from the linearized equilibrium equations in the configuration $\mathcal{C}'$ those written in the configuration $\mathcal{C}$. The equilibrium equations for both configurations can be obtained via application of the Hamilton's variational principle

$$\delta\mathcal{H}(\mathbf{u},\delta\mathbf{u}) = \int_{t_1}^{t_2} \delta(\mathcal{K} - \mathcal{W} + \mathcal{V}_c + \mathcal{V}_{nc})\,\mathrm{d}t = 0 \tag{6}$$

where $\mathcal{K} = \frac{1}{2}\int_V \rho(\mathbf{x})\dot{\mathbf{u}}^2\,\mathrm{d}v$ is the kinetic energy, $\mathcal{W} = \int_V \boldsymbol{\epsilon}^{\mathrm{T}}(\mathbf{u})\mathbf{s}(\mathbf{u})\,\mathrm{d}v$ includes the stored and dissipated energies, $\mathcal{V}_c = \int_V \mathbf{u}^{\mathrm{T}}\mathbf{f}_c(\mathbf{x},t)\,\mathrm{d}v + \int_{\partial V}\mathbf{u}^{\mathrm{T}}\mathbf{t}_c(\mathbf{x},t)\,\mathrm{d}a$ is the work done by the external conservative volume and surface loads $\mathbf{f}_c(\mathbf{x},t)$ and $\mathbf{t}_c(\mathbf{x},t)$, respectively, and $\delta\mathcal{W}_{nc} = \int_{\partial V}\delta\mathbf{u}^{\mathrm{T}}\mathbf{t}_{nc}(\mathbf{u})\,\mathrm{d}a$ is the nonconservative virtual work done by the external deformation dependent loads $\mathbf{t}_{nc}(\mathbf{u})$. In the previous definitions V denotes the volume of the solid while ∂V its boundary surface. It should be remarked that the nonconservative external virtual work must be evaluated at the current configuration $\mathbf{x}'(\mathbf{u})$, which is unknown. Therefore, the spatial description should be used rigorously instead of the material description. However, if the increment in magnitude of the load is sufficiently small, the integration of the current load intensity can be performed with good accuracy over the surface of the prestressed configuration ∂V (Bathe, 1996).

The linearized variations of the internal and nonconservative external works are, respectively

$$D_{\mathbf{u}}\delta\mathcal{W}(\mathbf{u},\delta\mathbf{u}) = \int_V \delta\boldsymbol{\epsilon}_{NL}^{\mathrm{T}}(\mathbf{u})\boldsymbol{\sigma}^0(\mathbf{x})\,\mathrm{d}v + \int_V\int_{-\infty}^{t}\delta\boldsymbol{\epsilon}_L^{\mathrm{T}}(\mathbf{u})\mathbb{D}^0((\mathbf{x}),t-\tau)\frac{\partial\boldsymbol{\epsilon}_L(\mathbf{u}(\mathbf{x},\tau))}{\partial\tau}\,\mathrm{d}t\,\mathrm{d}v \tag{7}$$

$$D_{\mathbf{u}}\delta\mathcal{V}_{nc}(\mathbf{u},\delta\mathbf{u}) = \int_{\partial V}\delta\mathbf{u}^{\mathrm{T}}\frac{\partial\mathbf{t}_{nc}^0(\mathbf{u})}{\partial\mathbf{u}}\mathbf{u}\,\mathrm{d}a + \int_{\partial V}\delta\mathbf{u}^{\mathrm{T}}\frac{\partial\Delta\mathbf{t}_{nc}(\mathbf{u})}{\partial\mathbf{u}}\mathbf{u}\,\mathrm{d}a \tag{8}$$

where $\boldsymbol{\sigma}^0(\mathbf{x}) = \left[\sigma_{xx}^0,\ \sigma_{yy}^0,\ \sigma_{zz}^0,\ \sigma_{yz}^0,\ \sigma_{xz}^0,\ \sigma_{xy}^0\right]^{\mathrm{T}}$ is the vector collecting the symmetric components of the Cauchy stress tensor $\mathbb{T}^0(\mathbf{x})$ in the prestressed configuration, $\mathbf{t}_{nc}^0(\mathbf{u})$ denotes the vector of nonconservative loads in the prestressed configuration while $\Delta\mathbf{t}_{nc}(\mathbf{u})$ represents its corresponding increment.

Using Eqs. (7) and (8), after some algebra Eq. (6) leads to

$$\begin{aligned}\delta\mathcal{H}(\mathbf{u},\delta\mathbf{u}) = \int_{t_1}^{t_2}\int_V\Big(-\delta\mathbf{u}^{\mathrm{T}}\rho(\mathbf{x})\ddot{\mathbf{u}} - (\delta\boldsymbol{\epsilon}_{NL}(\mathbf{u}))^{\mathrm{T}}\boldsymbol{\sigma}^0(\mathbf{x}) + \delta\mathbf{u}^{\mathrm{T}}\Delta\mathbf{f}_c(\mathbf{x},t)\Big)\\ \times\,\mathrm{d}v\,\mathrm{d}t - \int_{t_1}^{t_2}\int_V\int_{-\infty}^{t}(\delta\boldsymbol{\epsilon}_L(\mathbf{u}))^{\mathrm{T}}\mathbb{D}^0(\mathbf{x},t-\tau)\frac{\partial\boldsymbol{\epsilon}_L(\mathbf{u}(\mathbf{x},\tau))}{\partial\tau}\\ \times\,\mathrm{d}\tau\,\mathrm{d}v\,\mathrm{d}t + \int_{t_1}^{t_2}\int_{\partial V}\delta\mathbf{u}^{\mathrm{T}}\Delta\mathbf{t}_c(\mathbf{x},t)\,\mathrm{d}a\,\mathrm{d}t\\ + \int_{t_1}^{t_2}\int_{\partial V}\delta\mathbf{u}^{\mathrm{T}}\Delta\mathbf{t}_{nc}(\mathbf{u})\,\mathrm{d}a\,\mathrm{d}t + \int_{t_1}^{t_2}\int_{\partial V}\delta\mathbf{u}^{\mathrm{T}}\\ \times\left(\frac{\partial\mathbf{t}_{nc}^0(\mathbf{u})}{\partial\mathbf{u}}\mathbf{u} + \frac{\partial\Delta\mathbf{t}_{nc}(\mathbf{u})}{\partial\mathbf{u}}\mathbf{u}\right)\mathrm{d}a\,\mathrm{d}t = 0\end{aligned} \tag{9}$$

which represents the basic system governing the dynamic of small oscillations of a three dimensional viscoelastic body subjected to an initial generic stress field.

3. Safe formulation for prestressed viscoelastic waveguides

3.1. Discretized quantities in the frequency-wavenumber domain

Given a longitudinal invariance, or periodicity, of both material and geometric characteristics of the waveguide in direction z, the discretization is performed in the prestressed configuration for the cross section only using a planar mesh of n_{el} bi-dimensional finite elements of area Ω^e, with 3 degrees of freedom per node associated to the three displacements components u_i. Assuming an in-plane linear mapping from the reference element identified by the area Ω^{ref} and boundary $\partial\Omega^{\mathrm{ref}}$ to the corresponding area Ω^e and boundary $\partial\Omega^e$ of the generic eth element, the semi-isoparametric representation results in an uncoupled description of the out-of-plane and in-plane motion.

The displacement vector at a certain point $\mathbf{x}^e = (x^e, y^e, 0)$ within the eth element is approximated as

$$\mathbf{u}^e(\xi,z,t) = \mathbf{N}(\xi)\mathbf{q}^e(z,t) \quad \mathbf{x}^e \in \Omega^e \tag{10}$$

$$\mathbf{u}^e(\eta,z,t) = \mathbf{H}(\eta)\mathbf{q}^e(z,t) \quad \mathbf{x}^e \in \partial\Omega^e \tag{11}$$

where $\mathbf{N}(\xi)$ and $\mathbf{H}(\eta)$ are the matrices containing the shape functions, which are taken linear in the natural coordinates $\xi = (\xi_1, \xi_2)$ and η on Ω^{ref} and $\partial\Omega^{\mathrm{ref}}$ respectively, while $\mathbf{q}^e(z,t)$ is the vector of nodal displacements (see Fig. 1). Considering a time harmonic displacement field with angular frequency ω, the wave equation can be contracted from the time coordinate t to the angular frequency ω and from the longitudinal coordinate z to the wavenumber κ_z using the time and spatial Fourier transforms

$$\bar{f}(z,\omega) = \mathcal{F}[f(z,t)](\omega) = \int_{-\infty}^{+\infty} f(z,t)\exp(-\mathrm{i}\omega t)\,\mathrm{d}t \tag{12}$$

$$\hat{f}(\kappa_z,t) = \mathcal{F}[f(z,t)](\kappa_z) = \int_{-\infty}^{+\infty} f(z,t)\exp(-\mathrm{i}\kappa_z z)\,\mathrm{d}z \tag{13}$$

where i denotes the imaginary unit. Since the Fourier transforms act only on the t and z dependent fields, each wavenumber $\kappa_z(\omega)$ (or, conversely, each angular frequency $\omega(\kappa_z)$) is projected on the x–y plane and the corresponding waveform propagating in the z-direction is captured by the in-plane mesh of the waveguide cross section.

Using the transformations in Eqs. (12) and (13) together with the fundamental property $\mathcal{F}[\mathrm{d}^n f(z,t)/\mathrm{d}t^n](\omega) = (\mathrm{i}\omega)^n\bar{f}(z,\omega)$, the displacement and acceleration vectors are defined as $\hat{\mathbf{u}}^e(\xi,\kappa_z,\omega) = \mathbf{N}(\xi)\hat{\mathbf{q}}^e(\kappa_z,\omega)$ and $\hat{\ddot{\mathbf{u}}}^e(\xi,\kappa_z,\omega) = -\omega^2\mathbf{N}(\xi)\hat{\mathbf{q}}^e(\kappa_z,\omega)$ on Ω^e respectively, while on the element's boundary domain $\partial\Omega^e$ one has $\hat{\mathbf{u}}^e(\eta,\kappa_z,\omega) = \mathbf{H}(\eta)\hat{\mathbf{q}}^e(\kappa_z,\omega)$. Applying the same transformations to the external volume and surface loads for the generic eth finite element, the corresponding quantities converted in the wavenumber-frequency domain become $\hat{\mathbf{f}}^e(\xi,\kappa_z,\omega)$ and $\hat{\mathbf{t}}^e(\eta,\kappa_z,\omega)$.

The transformed kinematic relation given in Eq. (1) is

$$\hat{\tilde{\boldsymbol{\epsilon}}}_L^e(\xi,\kappa_z,\omega) = [\boldsymbol{\mathcal{B}}_\xi(\xi) + \mathrm{i}\kappa_z\boldsymbol{\mathcal{B}}_z(\xi)]\hat{\tilde{\mathbf{q}}}^e(\kappa_z,\omega) \tag{14}$$

where

$$\boldsymbol{\mathcal{B}}_\xi(\xi) = \left[\mathcal{L}_x\frac{\partial\mathbf{N}(\xi)}{\partial\xi_1} + \mathcal{L}_y\frac{\partial\mathbf{N}(\xi)}{\partial\xi_2}\right] \quad\text{and}\quad \boldsymbol{\mathcal{B}}_z(\xi) = \mathcal{L}_z\mathbf{N}(\xi) \tag{15}$$

Similarly, the vector of nonlinear strain components given in Eq. (2) transformed in the wavenumber-frequency domain takes the form

$$\hat{\tilde{\boldsymbol{\epsilon}}}_{NL}^e(\xi,\kappa_z,\omega) = \frac{1}{2}\begin{bmatrix}\left(\hat{\tilde{\mathbf{q}}}^e\right)^{\mathrm{T}}\frac{\partial\mathbf{N}^{\mathrm{T}}}{\partial\xi_1}\frac{\partial\mathbf{N}}{\partial\xi_1}\hat{\tilde{\mathbf{q}}}^e\\ \left(\hat{\tilde{\mathbf{q}}}^e\right)^{\mathrm{T}}\frac{\partial\mathbf{N}^{\mathrm{T}}}{\partial\xi_2}\frac{\partial\mathbf{N}}{\partial\xi_2}\hat{\tilde{\mathbf{q}}}^e\\ -\kappa_z^2\left(\hat{\tilde{\mathbf{q}}}^e\right)^{\mathrm{T}}\mathbf{N}^{\mathrm{T}}\mathbf{N}\hat{\tilde{\mathbf{q}}}^e\\ 2\mathrm{i}\kappa_z\left(\hat{\tilde{\mathbf{q}}}^e\right)^{\mathrm{T}}\frac{\partial\mathbf{N}^{\mathrm{T}}}{\partial\xi_2}\mathbf{N}\hat{\tilde{\mathbf{q}}}^e\\ 2\mathrm{i}\kappa_z\left(\hat{\tilde{\mathbf{q}}}^e\right)^{\mathrm{T}}\frac{\partial\mathbf{N}^{\mathrm{T}}}{\partial\xi_1}\mathbf{N}\hat{\tilde{\mathbf{q}}}^e\\ 2\left(\hat{\tilde{\mathbf{q}}}^e\right)^{\mathrm{T}}\frac{\partial\mathbf{N}^{\mathrm{T}}}{\partial\xi_1}\frac{\partial\mathbf{N}}{\partial\xi_2}\hat{\tilde{\mathbf{q}}}^e\end{bmatrix} \tag{16}$$

If the material properties are assumed to be constant with the z-direction and over the element domain Ω^e, the Fourier transformed incremental stress–strain position in Eq. (5) yields to the well known relation (Christensen, 2010)

$$D_{\hat{\mathbf{u}}}\hat{\mathbf{S}}^e(\xi,\kappa_z,\omega)=\int_{-\infty}^{+\infty}\int_{-\infty}^{t}\mathbb{D}_e^0(t-\tau)\frac{\partial\hat{\boldsymbol{\epsilon}}_L^e(\boldsymbol{\xi},\kappa_z,\tau)}{\partial\tau}\exp(-\mathrm{i}\omega t)\,\mathrm{d}\tau\,\mathrm{d}t = \bar{\mathbb{D}}_e^0(\mathrm{i}\omega)\hat{\boldsymbol{\epsilon}}_L^e(\boldsymbol{\xi},\kappa_z,\omega) \tag{17}$$

which states that the incremental stress relative to small deformations can be obtained in the wavenumber-frequency domain as in a linear elastic analysis, providing only the substitution of the real tensor of elastic moduli with the complex tensor of relaxation functions $\bar{\mathbb{D}}_e^0(\mathrm{i}\omega)=\Re(\bar{\mathbb{D}}_e^0(\omega))+\mathrm{i}\Im(\bar{\mathbb{D}}_e^0(\omega))$, where $\Re(\bar{\mathbb{D}}_e^0(\omega))$ is the so-called tensor of storage moduli and $\Im(\bar{\mathbb{D}}_e^0(\omega))$ denotes the tensor of loss moduli. If, instead, the material is assumed to be elastic, the tensor of the elastic constants $\mathbb{D}_e^0$ is independent of time and therefore not affected by the time–frequency contraction.

The discretized equations of motion can be derived for an infinite long waveguide by observing first that the relationship between an infinitesimal volume $\mathrm{d}v=\mathrm{d}x\,\mathrm{d}y\,\mathrm{d}z$ and the corresponding volume in the reference system $\mathrm{d}\xi_1\mathrm{d}\xi_2\mathrm{d}z$ is given by $\mathrm{d}x\,\mathrm{d}y\,\mathrm{d}z=J_v^e\mathrm{d}\xi_1\,\mathrm{d}\xi_2\,\mathrm{d}z$, with $J_v^e=\det\left[\frac{\partial(x,y)}{\partial(\xi_1,\xi_2)}\right]$ denoting the Jacobian of the isoparametric mapping in the x–y plane. Using these relations, one can compute each element volume integral in Eq. (9) as $\int_{\mathcal{V}^e}\mathrm{d}v=\int_{-\infty}^{+\infty}\mathrm{d}z\int_{\Omega^e}J_v^e\,\mathrm{d}\xi_1\,\mathrm{d}\xi_2$, where the integration over the z-coordinate remains unaltered.

Similarly, the relation between an infinitesimal area of the waveguide in the prestressed and reference states can be written as $\mathrm{d}a=\mathrm{d}s\,\mathrm{d}z=J_a^e\mathrm{d}\eta\mathrm{d}z$, where the Jacobian of the in-plane transformation is now given by $J_a^e=\left\|\frac{\partial\mathbf{x}^e}{\partial\eta}\times\mathbf{n}_3\right\|$, where $\mathbf{n}_3$ denotes the unit vector along the z-direction. Therefore, each surface integral in Eq. (9) can be written as $\int_{\partial\mathcal{V}^e}\mathrm{d}a=\int_{-\infty}^{+\infty}\mathrm{d}z\int_{\partial\Omega^e}J_a^e\,\mathrm{d}\eta$, where again the integration along the z-direction remains unaltered.

Substituting Eqs. (14), (16) and (17) into Eq. (9), after some algebra the following linear system of M equations in the (κ_z,ω) domain can be obtained

$$\left[\kappa_z^2\mathbf{K}_3-\mathrm{i}\kappa_z\mathbf{K}_2+\mathbf{K}_1-\omega^2\mathbf{M}\right]\hat{\mathbf{Q}}(\kappa_z,\omega)=\mathbf{0} \tag{18}$$

where $\hat{\mathbf{Q}}(\kappa_z,\omega)=\bigcup_{e=1}^{n_{el}}\hat{\mathbf{q}}^e(\kappa_z,\omega)$ is the global vector of nodal displacements, while $\mathbf{M}=\bigcup_{e=1}^{n_{el}}\mathbf{m}^e$ is the global mass matrix. The operator $\bigcup_{e=1}^{n_{el}}$ means that each global quantity is obtained via the application of a finite element assembling procedure for all the n_{el} elements of the mesh. The stiffness operators $\mathbf{K}_i$

$$\begin{aligned}
\mathbf{K}_3&=\bigcup_{e=1}^{n_{el}}\left[\mathbf{k}_3^e+\mathbf{k}_{\sigma_{zz}^0}^e\right]\\
\mathbf{K}_2&=\bigcup_{e=1}^{n_{el}}\left[\mathbf{k}_2^e-\left(\mathbf{k}_2^e\right)^{\mathrm{T}}+\mathbf{k}_{\sigma_{yz}^0}^e-\left(\mathbf{k}_{\sigma_{yz}^0}^e\right)^{\mathrm{T}}+\mathbf{k}_{\sigma_{xz}^0}^e-\left(\mathbf{k}_{\sigma_{xz}^0}^e\right)^{\mathrm{T}}\right]\\
\mathbf{K}_1&=\bigcup_{e=1}^{n_{el}}\left[\mathbf{k}_1^e+\mathbf{k}_{\sigma_{xx}^0}^e+\mathbf{k}_{\sigma_{yy}^0}^e+\mathbf{k}_{\sigma_{xy}^0}^e+\left(\mathbf{k}_{\sigma_{xy}^0}^e\right)^{\mathrm{T}}\right]-\bigcup_{r=1}^{n_r}\mathbf{k}_{nc}^r
\end{aligned} \tag{19}$$

are derived by assembling the corresponding stiffness quantities at the element level, which are

$$\begin{aligned}
\mathbf{k}_3^e&=\int_{\Omega^{\mathrm{ref}}}\boldsymbol{\mathcal{B}}_z^{\mathrm{T}}\bar{\mathbb{D}}_e^0(\mathrm{i}\omega)\boldsymbol{\mathcal{B}}_z J_v^e\,\mathrm{d}\xi_1\,\mathrm{d}\xi_2, &\qquad \mathbf{k}_2^e&=\int_{\Omega^{\mathrm{ref}}}\boldsymbol{\mathcal{B}}_\xi^{\mathrm{T}}\bar{\mathbb{D}}_e^0(\mathrm{i}\omega)\boldsymbol{\mathcal{B}}_z J_v^e\,\mathrm{d}\xi_1\,\mathrm{d}\xi_2\\
\mathbf{k}_1^e&=\int_{\Omega^{\mathrm{ref}}}\boldsymbol{\mathcal{B}}_\xi^{\mathrm{T}}\bar{\mathbb{D}}_e^0(\mathrm{i}\omega)\boldsymbol{\mathcal{B}}_\xi J_v^e\,\mathrm{d}\xi_1\,\mathrm{d}\xi_2, &\qquad \mathbf{m}^e&=\int_{\Omega^{\mathrm{ref}}}\rho_e\mathbf{N}^{\mathrm{T}}\mathbf{N}J_v^e\,\mathrm{d}\xi_1\,\mathrm{d}\xi_2\\
\mathbf{k}_{\sigma_{xx}^0}^e&=\int_{\Omega^{\mathrm{ref}}}\sigma_{xx}^0(\boldsymbol{\xi})\frac{\partial\mathbf{N}^{\mathrm{T}}}{\partial\xi_1}\frac{\partial\mathbf{N}}{\partial\xi_1}J_v^e\,\mathrm{d}\xi_1\,\mathrm{d}\xi_2\\
\mathbf{k}_{\sigma_{yy}^0}^e&=\int_{\Omega^{\mathrm{ref}}}\sigma_{yy}^0(\boldsymbol{\xi})\frac{\partial\mathbf{N}^{\mathrm{T}}}{\partial\xi_2}\frac{\partial\mathbf{N}}{\partial\xi_2}J_v^e\,\mathrm{d}\xi_1\,\mathrm{d}\xi_2\\
\mathbf{k}_{\sigma_{zz}^0}^e&=\int_{\Omega^{\mathrm{ref}}}\sigma_{zz}^0(\boldsymbol{\xi})\mathbf{N}^{\mathrm{T}}\mathbf{N}J_v^e\,\mathrm{d}\xi_1\,\mathrm{d}\xi_2\\
\mathbf{k}_{\sigma_{yz}^0}^e&=\int_{\Omega^{\mathrm{ref}}}\sigma_{yz}^0(\boldsymbol{\xi})\frac{\partial\mathbf{N}^{\mathrm{T}}}{\partial\xi_2}\mathbf{N}J_v^e\,\mathrm{d}\xi_1\,\mathrm{d}\xi_2\\
\mathbf{k}_{\sigma_{xz}^0}^e&=\int_{\Omega^{\mathrm{ref}}}\sigma_{xz}^0(\boldsymbol{\xi})\frac{\partial\mathbf{N}^{\mathrm{T}}}{\partial\xi_1}\mathbf{N}J_v^e\,\mathrm{d}\xi_1\,\mathrm{d}\xi_2\\
\mathbf{k}_{\sigma_{xy}^0}^e&=\int_{\Omega^{\mathrm{ref}}}\sigma_{xy}^0(\boldsymbol{\xi})\frac{\partial\mathbf{N}^{\mathrm{T}}}{\partial\xi_1}\frac{\partial\mathbf{N}}{\partial\xi_2}J_v^e\,\mathrm{d}\xi_1\,\mathrm{d}\xi_2
\end{aligned} \tag{20}$$

The integration of these quantities can be performed in a straightforward manner via Gauss quadrature rules (Wriggers, 2008). The algebraic system in Eq. (18) is presented only in its homogeneous part (omitting thus the external loads contributes) for the purpose of the dispersive curves extraction, which is covered in the next section. It should be observed that this system does not represent a complete general form of the possible load conditions as it has been derived making the assumption of invariant initial stresses along the z direction. In some practical situations this statement may not be representative of the actual stress distribution in the waveguide. In these situations, the various operators defined in Eq. (20) still remain formally unchanged but their positions inside the final system of Eq. (18) may vary.

Further considerations can be made concerning the nonconservative forces applied to the system, which in the following are assumed to be of pressure-type only with no friction between the solid–fluid interfaces. In this case one can recognize that $\mathbf{t}_{nc}=-p\mathbf{n}$, where p is the pressure applied to the surface of external normal $\mathbf{n}$ (see Fig. 1).

If the fluid–structure interaction is neglected, then the second term on the right hand side of Eq. (8) vanishes since the magnitude of the pressure does not depend upon the deformation, but only on the load direction $p\mathbf{n}(\mathbf{u})$. It follows that the linearized external virtual work can be re-expressed as

$$D_{\mathbf{u}}\delta\mathcal{V}_p(\mathbf{u},\delta\mathbf{u})=\int_{\partial\Omega}-p_0\delta\mathbf{u}^{\mathrm{T}}(D_{\mathbf{u}}\mathbf{n}(\mathbf{u}))\,\mathrm{d}a \tag{21}$$

where p_0 is the hydrostatic pressure in the prestressed configuration and $D_{\mathbf{u}}\mathbf{n}(\mathbf{u})$ denotes the linearized change of orientation of the surface normal due to the displacement $\mathbf{u}$ at the same point. The surface integral in Eq. (21) can be reduced to a line integral over the boundary of the reference element $\partial\Omega^{\mathrm{ref}}$ by introducing the linearization (Wriggers, 2008; Bonet and Wood, 2008)

$$D_{\mathbf{u}}\mathbf{n}(\mathbf{u})=\frac{\frac{\partial\mathbf{u}}{\partial\eta}\times\mathbf{n}_3}{\left\|\frac{\partial\mathbf{x}}{\partial\eta}\times\mathbf{n}_3\right\|} \tag{22}$$

which require a counterclockwise numeration of the element nodes of the mesh in order to ensure the positiveness of the sign of the outward normal $\mathbf{n}(\mathbf{u})$. Substituting Eq. (22) into Eq. (21) allows to rewrite the incremental nonconservative virtual work for the finite element mesh as follows

$$\begin{aligned}
D_{\mathbf{u}}\delta\mathcal{V}_p(\mathbf{u},\delta\mathbf{u})&=\bigcup_{r=1}^{n_r}\int_{\partial\Omega^{\mathrm{ref}}}-p_0\delta\mathbf{u}^{\mathrm{T}}\frac{\left(\frac{\partial\mathbf{u}}{\partial\eta}\times\mathbf{n}_3\right)}{\left\|\frac{\partial\mathbf{x}}{\partial\eta}\times\mathbf{n}_3\right\|}J_a^e\,\mathrm{d}\eta\\
&=\bigcup_{r=1}^{n_r}(\delta\mathbf{q}^r)^{\mathrm{T}}\int_{\partial\Omega^{\mathrm{ref}}}-p_0\mathbf{H}^{\mathrm{T}}\left(\frac{\partial\mathbf{H}}{\partial\eta}\mathbf{q}^r\times\mathbf{n}_3\right)\mathrm{d}\eta=\delta\mathbf{Q}^{\mathrm{T}}\mathbf{K}_p\mathbf{Q}
\end{aligned} \tag{23}$$

where n_r is the total number of elements with edges belonging to the cross section boundary. The global pressure stiffness matrix $\mathbf{K}_p$ is formed by assembling each element's stiffness contribute $\mathbf{k}_p^r$ in the usual manner, with

$$\mathbf{k}_p^r=\int_{\partial\Omega^{\mathrm{ref}}}-p_0\mathbf{H}^{\mathrm{T}}\begin{bmatrix}0&1&0\\-1&0&0\\0&0&0\end{bmatrix}\frac{\partial\mathbf{H}}{\partial\eta}\,\mathrm{d}\eta. \tag{24}$$

It should be noted that the particular case of closed surface and constant pressure preserves the symmetry of $\mathbf{K}_p$, that is in general non symmetric. In force of this property, one can assume an incremental pressure pseudo potential $D_{\mathbf{u}}\mathcal{V}_p=\frac{1}{2}\mathbf{Q}^{\mathrm{T}}\mathbf{K}_p\mathbf{Q}$, which is the particular case of nonconservative work considered in the rest of this work. Noting that the operator in Eq. (24) is real and independent from z, and therefore not affected by the time and space contractions,

the above pseudo potential is readily obtained in the (κ_z, ω) domain by substituting the real eigenvectors with the corresponding complex ones.

3.2. Dispersion analysis

The homogeneous system in Eq. (18) leads to a polynomial eigenvalue problem which can be converted into the state space and solved in the wavenumbers $\kappa_z^m(\omega) = \Re(\kappa_z^m) + \mathrm{i}\Im(\kappa_z^m)$, $(m = 1, \ldots, 2M)$ for any given real positive value of the angular frequency ω. The corresponding eigenvector $\hat{\hat{\mathbf{Q}}}^m = \Re(\hat{\hat{\mathbf{Q}}}^m) + \mathrm{i}\Im(\hat{\hat{\mathbf{Q}}}^m)$ defines the mth mode shape of the waveguide, while dispersive quantities, i.e. phase velocity, group velocity and attenuation, are related to the wavenumber $\kappa_z^m(\omega)$ via the expressions $c_p^m(\omega) = \omega/\Re(\kappa_z^m)$, $c_{gr}^m(\omega) = \partial\omega/\partial\kappa_z^m$ and $\alpha^m(\omega) = \Im(\kappa_z^m)$ respectively.

A closed formula for the computation of group velocity in lossless medium ($\Im(\kappa_z^m) = 0$) and for axial loads only ($\sigma_{zz}^0 \neq 0$) has been already discussed in the literature (Loveday, 2009; Loveday and Wilcox, 2010; Bartoli et al., 2010):

$$c_{gr}^m(\omega) = \frac{\partial\omega}{\partial\kappa_z^m} = \frac{\hat{\hat{\mathbf{Q}}}^{\mathrm{T}}\left[\mathbf{T}^{\mathrm{H}}\mathbf{K}_2\mathbf{T} + 2\kappa_z^m(\omega)\mathbf{K}_3\right]\hat{\hat{\mathbf{Q}}}}{2\omega\hat{\hat{\mathbf{Q}}}^{\mathrm{T}}\mathbf{M}\hat{\hat{\mathbf{Q}}}} \tag{25}$$

Such formula is still valid for the case of general initial stress, with the exception that the operator $\mathbf{K}_i$ inglobes also the geometric stiffness terms related to the nonzero initial stress components σ_{yz}^0 and σ_{xz}^0 as defined in Eq. (19). In Eq. (25) $\mathbf{T}$ is an $M \times M$ identity matrix with the imaginary unit substituted in correspondence of each degree of freedom in the z direction and H denotes the complex conjugate transpose (Hermitian).

As well stated in the literature (Brillouin, 1960; Whitam, 1974; Achenbach, 1973), the equivalence between the group velocity c_{gr} and the velocity of energy transportation c_e is guaranteed by the Lighthill theorem (Biot, 1957; Lighthill, 1965) only in the general case of dispersive uniform lossless media, for which the central wavenumber of the wave packets traveling at infinitely close frequencies is conserved. On the contrary, the dissipation mechanism in nonconservative systems leads to complex wavenumbers and, as a consequence, the group velocity loses significance and the meaningful parameter becomes the energy velocity (Gerasik and Stastna, 2010; Davidovich, 2010).

3.3. Energy velocity

The rate of transfer of the energy is determined as the ratio between the energy flux density per unit of time and the total energy density of the system, which follows from the application of the energy conservation law (Chang and Ho, 1995; Holzapfel, 2000)

$$\frac{\mathrm{D}\mathcal{K}}{\mathrm{D}t} + \mathcal{P}_{\mathrm{int}} + \mathcal{P}_D = \mathcal{P}_{\mathrm{ext}}^v + \mathcal{P}_{\mathrm{ext}}^s \tag{26}$$

where the stress power $\mathcal{P}_{\mathrm{int}}$, the viscous power loss $\mathcal{P}_D$, the power supplied on the system by the external volume forces $\mathcal{P}_{\mathrm{ext}}^v$ and the power supplied by the external surface forces, $\mathcal{P}_{\mathrm{ext}}^s$, are expressed, in the order, as

$$\mathcal{P}_{\mathrm{int}} + \mathcal{P}_D = \int_V \mathbb{P}(\mathbf{u}) : \dot{\mathbb{F}}(\mathbf{u})\,\mathrm{d}v \tag{27}$$

$$\mathcal{P}_{\mathrm{ext}}^v = \int_V \dot{\mathbf{u}}^{\mathrm{T}}\mathbf{f}_c\,\mathrm{d}v \tag{28}$$

$$\mathcal{P}_{\mathrm{ext}}^s = \int_{\partial V} \dot{\mathbf{u}}^{\mathrm{T}}(\mathbf{t}_c - p\mathbf{n})\,\mathrm{d}a \tag{29}$$

where $\mathbb{P}(\mathbf{u})$ is the 1st Piola–Kirchhoff stress tensor and $\mathbb{F}(\mathbf{u}) = \frac{\partial \mathbf{x}'(\mathbf{u})}{\partial \mathbf{x}}$ is the deformation gradient. Eq. (26) can be recasted in linear incremental form by introducing the positions in Eqs. (27)–(29) and applying the usual linearization concept. Using the power equivalence $\int_V \mathbb{P}(\mathbf{u}) : \dot{\mathbb{F}}(\mathbf{u})\,\mathrm{d}v = \int_V \mathbb{S}(\mathbf{u}) : \dot{\mathbb{E}}(\mathbf{u})\,\mathrm{d}v$ and considering a constant pressure p_0 applied to closed boundary conditions during the motion (i.e. no fluid–structure interaction), yields to

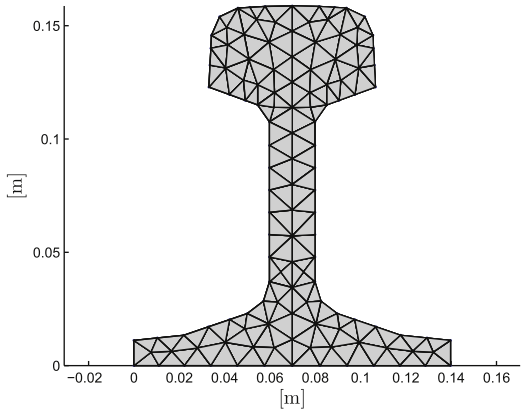

Fig. 2. Finite element mesh used for the dispersion curves extraction in Sections 4.1 and 4.2.

$$\frac{\partial}{\partial t}\left(\Delta\mathcal{K} + D_{\mathbf{u}}\mathcal{W} - D_{\mathbf{u}}\mathcal{V}_p\right) = \int_V \dot{\mathbf{u}}^{\mathrm{T}}\Delta\mathbf{f}_c(t)\,\mathrm{d}v + \int_{\partial V} \dot{\mathbf{u}}^{\mathrm{T}}\Delta\mathbf{t}_c(t)\,\mathrm{d}a \tag{30}$$

which represents the incremental form of the balance of energy in material description. Looking at the second integral on the right hand side of Eq. (30) in terms of incremental equilibrium at the boundary surface of the solid, it can be recognized that $D_{\mathbf{u}}\mathbb{P}(\mathbf{u})\mathbf{n} = \Delta\mathbf{t}_c(t)$ where, in force of the relations

$$\begin{aligned}
&\mathbb{P}(\mathbf{u}) = \mathbb{F}(\mathbf{u})\mathbb{S}(\mathbf{u}),\\
&D_{\mathbf{u}}\mathbb{F}(\mathbf{u}) = \nabla\mathbf{u},\\
&\mathbb{S}(\mathbf{u})|_{\mathbf{u}=0} = \mathbb{T}^0(\mathbf{x}),\\
&\mathbb{F}(\mathbf{u})|_{\mathbf{u}=0} = \mathbf{I},\\
&\mathbb{E}_L(\mathbf{u}) = \mathrm{sym}(\nabla\mathbf{u}),\\
&D_{\mathbf{u}}\mathbb{S}(\mathbf{u}) = \mathbb{D}^0(t-\tau) : \mathbb{E}_L(\mathbf{u})
\end{aligned} \tag{31}$$

the linearized 1st Piola–Kirchhoff stress tensor takes the form

$$D_{\mathbf{u}}\mathbb{P}(\mathbf{u}) = \nabla\mathbf{u}\mathbb{T}^0(\mathbf{x}) + \int_{-\infty}^{t} \mathbb{D}^0(t-\tau) : \frac{\partial\mathbb{E}_L(\mathbf{u}(\mathbf{x},\tau))}{\partial\tau}\,\mathrm{d}\tau \tag{32}$$

Multiplication of Eq. (32) by $\mathbf{n}$ and substitution inside the boundary integral on the right hand side of Eq. (30) leads finally to the incremental form of the Poynting theorem in material description

$$\frac{\partial}{\partial t}\left(\Delta\mathcal{K} + D_{\mathbf{u}}\mathcal{W} - D_{\mathbf{u}}\mathcal{V}_p\right) + \int_{\partial V} -(D_{\mathbf{u}}\mathbb{P}(\mathbf{u}))^{\mathrm{T}}\dot{\mathbf{u}}\cdot\mathbf{n}\,\mathrm{d}a = \Delta\mathcal{P}_{\mathrm{ext}}^v \tag{33}$$

where $-(D_{\mathbf{u}}\mathbb{P}(\mathbf{u}))^{\mathrm{T}}\dot{\mathbf{u}}$ is the incremental energy flux vector in material description, also known as the acoustic Poynting vector in incremental form.

Given the harmonic behavior of the wave process, the time derivative can be replaced by the average over a time period $[t, t + 2\pi/\omega]$, leading to

$$\left\langle \Delta\hat{\hat{\mathcal{K}}} + D_{\hat{\mathbf{u}}}\hat{\hat{\mathcal{V}}} - D_{\dot{\hat{\mathbf{u}}}}\hat{\hat{\mathcal{V}}}_p \right\rangle + \int_{\partial V} \left\langle D_{\dot{\hat{\mathbf{u}}}}\hat{\hat{\mathbf{J}}}(\hat{\hat{\mathbf{u}}})\cdot\mathbf{n} \right\rangle \mathrm{d}a = \left\langle \Delta\hat{\hat{\mathcal{P}}}_{\mathrm{ext}}^v \right\rangle \tag{34}$$

where $\langle\rangle = \frac{\omega}{2\pi}\int_t^{t+\frac{2\pi}{\omega}} \mathrm{d}t$ denotes the time average operation and the incremental Poynting vector $D_{\dot{\hat{\mathbf{u}}}}\hat{\hat{\mathbf{J}}}(\hat{\hat{\mathbf{u}}}) = -(D_{\dot{\hat{\mathbf{u}}}}\hat{\hat{\mathbb{P}}}(\hat{\hat{\mathbf{u}}}))^{\mathrm{T}}\dot{\hat{\hat{\mathbf{u}}}}$ in the frequency-wavenumber domain takes the form

$$D_{\dot{\hat{\mathbf{u}}}}\hat{\hat{\mathbf{J}}}(\hat{\hat{\mathbf{u}}}) = -\mathrm{i}\omega\left[\mathbb{T}^0(\mathbf{x}), y(\nabla\hat{\hat{\mathbf{u}}})^{\mathrm{T}} + \bar{\mathbb{D}}^0(\omega) : \hat{\hat{\mathbb{E}}}_L(\hat{\hat{\mathbf{u}}})\right]\hat{\hat{\mathbf{u}}} \tag{35}$$

Once the wave solution is known from the eigenvalue problem of Eq. (18) in terms of κ_z^m and $\hat{\hat{\mathbf{Q}}}^m$ for the mth propagating mode, the previous quantities are only function of the angular frequency ω.

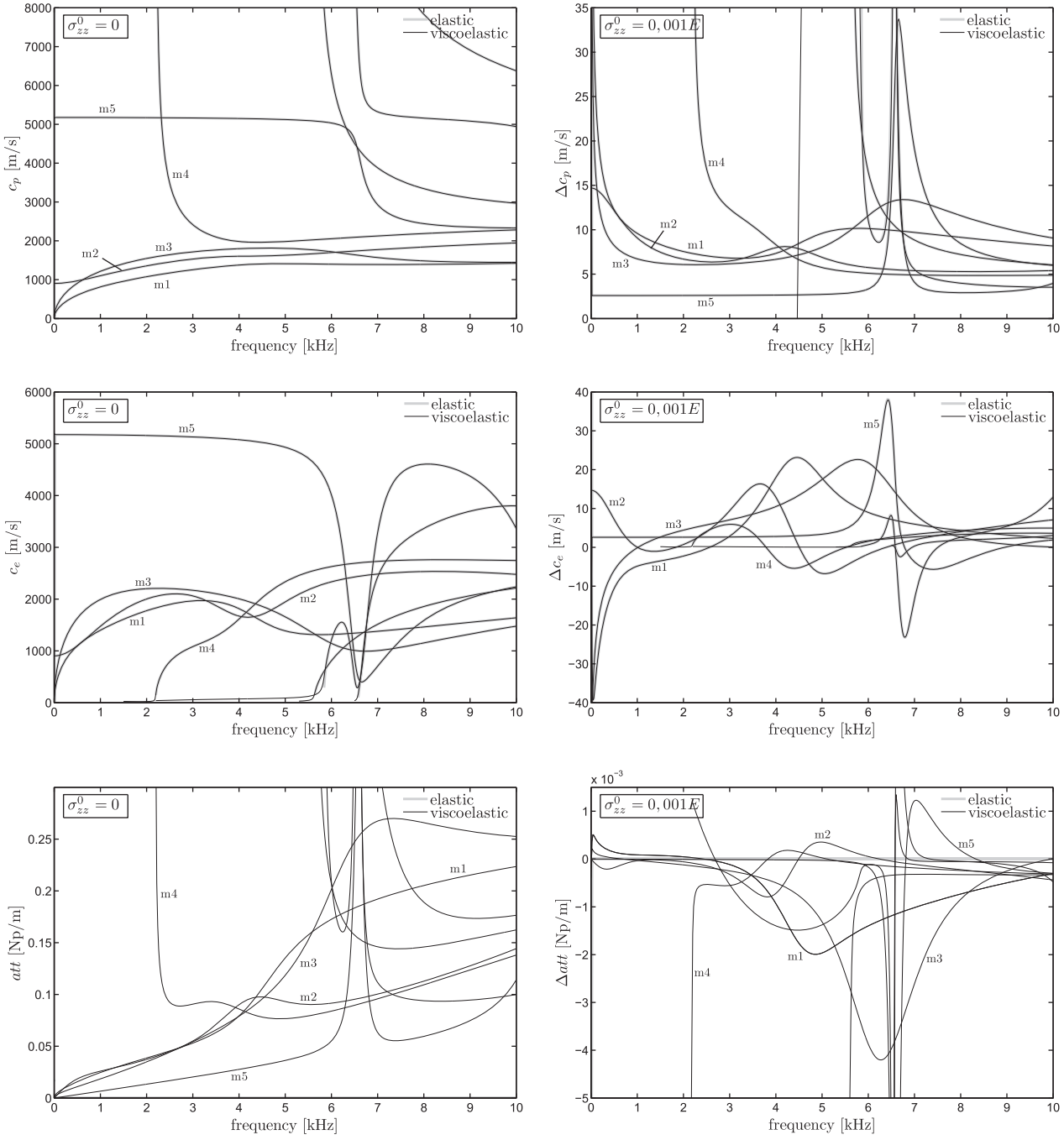

Fig. 3. Phase velocity, energy velocity and attenuation for the loaded and unloaded cases. The first five modes $m1$, $m2$, $m3$, $m4$ and $m5$ are identified as in Bartoli et al. (2006).

Based on the Umov's definition (Davidovich, 2010), the energy velocity for the mth propagating mode is then obtained as the ratio between the average energy flux component projected along the z-direction and the total energy density of the waveguide at the given angular frequency ω

$$c_e^m(\omega) = \frac{\int_\Omega \left\langle D_{\hat{\mathbf{u}}}\hat{\mathbf{J}}^m(\omega)\cdot\mathbf{n}_3\right\rangle \mathrm{d}\Omega}{\left\langle \Delta\hat{\mathcal{K}}^m(\omega) + D_{\hat{\mathbf{u}}}\hat{\mathcal{W}}^m(\omega)\right\rangle\Big|_\Omega - \left\langle D_{\hat{\mathbf{u}}}\hat{\mathcal{V}}_p^m(\omega)\right\rangle\Big|_{\partial\Omega}} \tag{36}$$

As shown in other works (Treyssède, 2008), Eq. (36) can be rewritten making use of the matrix operators previously defined. For the incremental energy flux in the z direction, using Eq. (35) and the compatibility operator $\mathcal{L}_z$, one obtains

$$\left\langle D_{\hat{\mathbf{u}}}\hat{\mathbf{J}}^m(\omega)\cdot\mathbf{n}_3\right\rangle = \frac{\omega}{2}\Im\left[\left(\hat{\mathbf{u}}^m\right)^{\mathrm{H}}\left(\sigma^0_{13}\frac{\partial\hat{\mathbf{u}}^m}{\partial x} + \sigma^0_{23}\frac{\partial\hat{\mathbf{u}}^m}{\partial y} + \mathrm{i}\kappa_z^m(\omega)\sigma^0_{33}\hat{\mathbf{u}}^m + \boldsymbol{\mathcal{L}}_z^{\mathrm{T}}\bar{\mathbb{D}}^0\hat{\boldsymbol{\epsilon}}_L^m\right)\right] \tag{37}$$

Substituting the expression in Eq. (10) and recalling the operators in Eq. (20), the integral of the energy intensity flux over the waveguide cross section reads

$$\int_\Omega \left\langle D_{\hat{\mathbf{u}}}\hat{\mathbf{J}}^m(\omega)\cdot\mathbf{n}_3\right\rangle \mathrm{d}\Omega = \frac{\omega}{2}\Im\left\{\left(\hat{\mathbf{Q}}^m\right)^{\mathrm{H}}\left[\mathbf{K}^{\mathrm{T}}_{\sigma^0_{xz}} + \mathbf{K}^{\mathrm{T}}_{\sigma^0_{yz}} + \mathbf{K}_2^{\mathrm{T}} + \mathrm{i}\kappa_z^m(\omega)\left(\mathbf{K}_3 + \mathbf{K}_{\sigma^0_{zz}}\right)\right]\hat{\mathbf{Q}}^m\right\} \tag{38}$$

while the time average incremental kinetic energy, stored and dissipated energy, as well as the average nonconservative work are defined respectively as

$$\left\langle \Delta\hat{\mathcal{K}}^m(\omega)\right\rangle\Big|_\Omega = \frac{\omega^2}{4}\Re\left[\left(\hat{\mathbf{Q}}^m\right)^{\mathrm{H}}\mathbf{M}\hat{\mathbf{Q}}^m\right] \tag{39}$$

$$\left\langle D_{\mathbf{u}}\hat{\mathcal{W}}^m(\omega)\right\rangle\Big|_\Omega = \frac{1}{4}\Re\Big\{\left(\hat{\mathbf{Q}}^m\right)^{\mathrm{H}}\Big[\left(\kappa_z^m(\omega)\right)^2\left(\mathbf{K}_3+\mathbf{K}_{\sigma^0_{zz}}\right) + \mathrm{i}\kappa_z^m(\omega)\left(\mathbf{K}_2-\mathbf{K}_2^{\mathrm{T}}+2\mathbf{K}_{\sigma^0_{yz}}+2\mathbf{K}_{\sigma^0_{xz}}\right)+\mathbf{K}_1+\mathbf{K}_{\sigma^0_{xx}}+\mathbf{K}_{\sigma^0_{yy}}+2\mathbf{K}_{\sigma^0_{xy}}\Big]\hat{\mathbf{Q}}^m\Big\} \tag{40}$$

$$\left\langle D_{\mathbf{u}}\hat{\mathcal{V}}_p^m(\omega)\right\rangle\Big|_{\partial\Omega} = \frac{1}{4}\Re\left[\left(\hat{\mathbf{Q}}^m\right)^{\mathrm{H}}\mathbf{K}_p\hat{\mathbf{Q}}^m\right]. \tag{41}$$

Substituting Eqs. (38)–(41) into Eq. (36) provides the energy velocity for the assumed mth wave at given frequency ω. This relation holds for a generic 3D prestress field and linear elastic and viscoelastic materials. Moreover, it can be verified that Eq. (25) is exactly recovered by Eq. (36) for the case of non dissipative (lossless) materials.

4. Numerical applications

4.1. Viscoelastic rail under thermal-induced axial stress

Residual stresses represent a fundamental issue in the railway production and maintenance since they affect negatively the rail resistance, compromise integrity and reduce durability. While the presence of high compressive stresses is generally related to buckling problems, especially under hot temperatures, tensile stresses represent a vehicle for crack initiation and propagation. Moreover, some geometrical characteristics of the rail such as straightness and flatness of the running surface can be deteriorated with loss in comfort. Therefore, it is of great importance for railways companies to monitor the state of stress of the whole rail.

Some numerical investigations on the effect of a constant axial prestress σ^0_{zz} along with some proposed techniques based on guided waves for the stress magnitude measurement can be found in Chen and Wilcox (2007), Loveday (2009), Loveday and Wilcox (2010) and Bartoli et al. (2010). In these works only perfectly elastic materials are considered. The purpose of this numerical example is to show the effect of the material attenuation on the dispersive behavior of guided waves propagating in the rail subjected to a positive axial elongation $\varepsilon^0_{zz} = 0.1\%$.

In the following examples a standard A113 rail is considered. The mesh used is represented in Fig. 2, which is composed of 125 nodes and 182 triangular elements with linear shape functions. The steel in the prestressed configuration is considered as a hysteretic linear viscoelastic material with mass density $\rho = 7800\ \mathrm{kg/m^3}$, longitudinal and shear bulk waves equal to $c_L = 6005$ m/s and $c_S = 3210$ m/s respectively, longitudinal bulk wave attenuation $\kappa_L = 0.003\ \mathrm{Np}/\lambda$ and shear bulk wave attenuation $\kappa_S = 0.043\ \mathrm{Np}/\lambda$. The complex bulk velocities, Young's modulus and Poisson's ratio can be expressed, accordingly to Bartoli et al. (2006), as

$$\bar{c}_{L,S} = c_{L,S}\left(1+\mathrm{i}\frac{\kappa_{L,S}}{2\pi}\right)^{-1},\quad \bar{E} = \rho\bar{c}_S\left(\frac{3\bar{c}_L^2-4\bar{c}_S^2}{\bar{c}_L^2-\bar{c}_S^2}\right),\quad \bar{\nu} = \frac{1}{2}\left(\frac{\bar{c}_L^2-2\bar{c}_S^2}{\bar{c}_L^2-\bar{c}_S^2}\right) \tag{42}$$

from which one obtains the complex Lamè constants and the tensor of complex moduli

$$\bar{\lambda} = \frac{\bar{E}\bar{\nu}}{(1+\bar{\nu})(1-2\bar{\nu})},\quad \bar{\mu} = \frac{\bar{E}}{2(1+\bar{\nu})},$$
$$\bar{\mathbb{D}}^0_{ijkm} = \bar{\lambda}\delta_{ij}\delta_{km} + \bar{\mu}\left(\delta_{ik}\delta_{jm}+\delta_{im}\delta_{jk}\right) \tag{43}$$

to be used into the incremental stress–strain relations in Eq. (17). It should be noted that the tensor of complex moduli remains independent from the angular frequency ω, in agreement with the assumed hysteretic behavior of the material. Therefore, there is no need to update it at each frequency step performed in the eigenvalue problem of Eq. (18) and each stiffness operator defined in Eq. (20), as well as the matrix operator, can be computed once at the beginning of the analysis.

The dispersion results in the $0 \div 10$ kHz frequency range are depicted in Fig. 3 for the first five low order modes. The mode identification assumed here is the same adopted in Bartoli et al. (2006), where the flexural-like modes $m1$ and $m4$ as well as the torsional-like mode $m2$ result to be antisymmetric with respect to the x–z plane while the flexural-like mode $m3$ and the extensional-like mode $m5$ are symmetric. The three plots represented

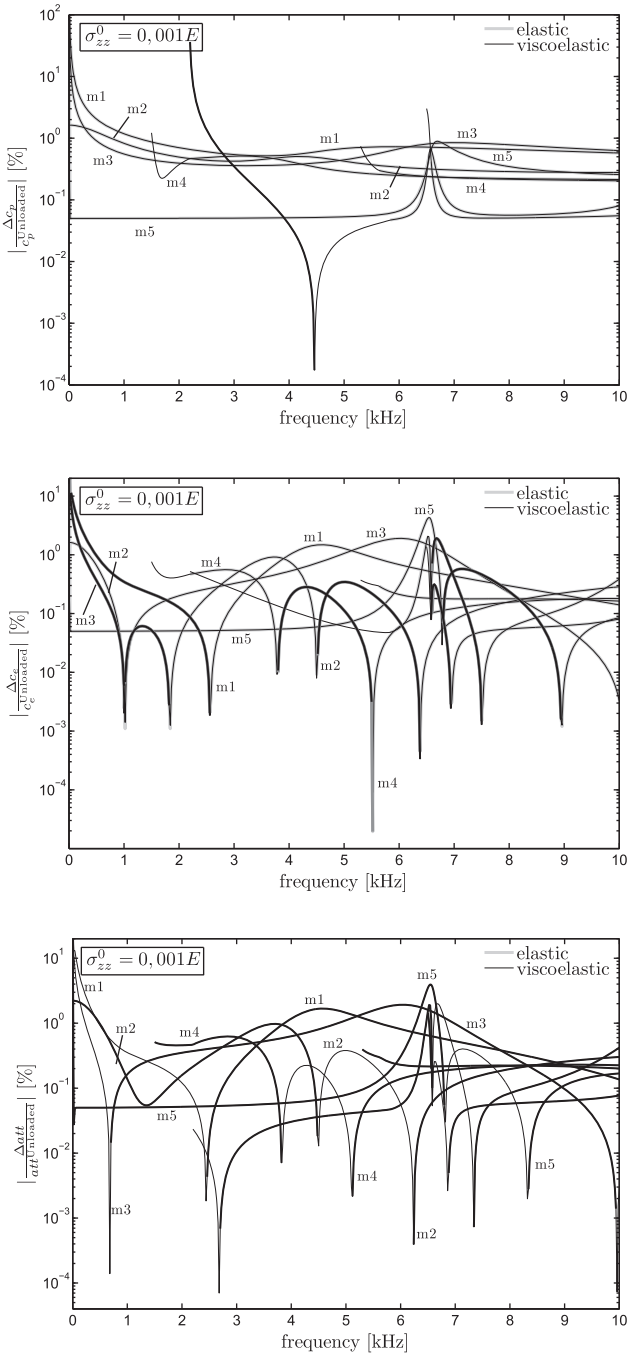

Fig. 4. Normalized phase velocity, energy velocity and attenuation variations between the unloaded and the axially loaded rail cases (elastic and viscoelastic). Thin lines denote positive variations while thick lines denote negative variations.

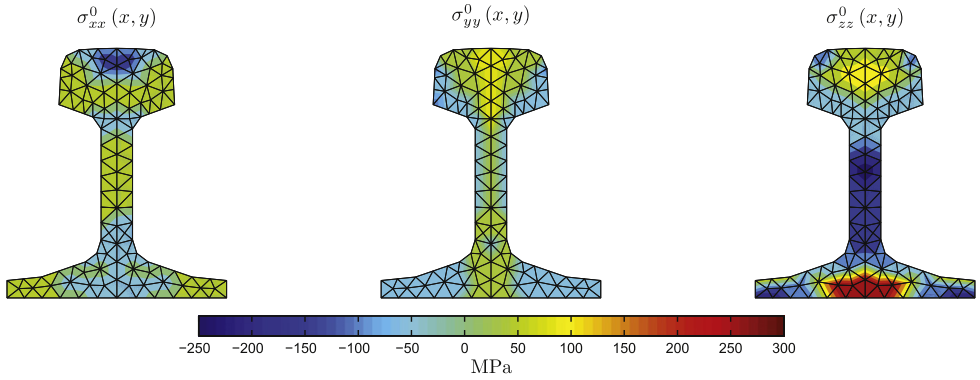

Fig. 5. Reconstructed stress patterns for the roller straightened 113A standard profile in Keller et al. (2003).

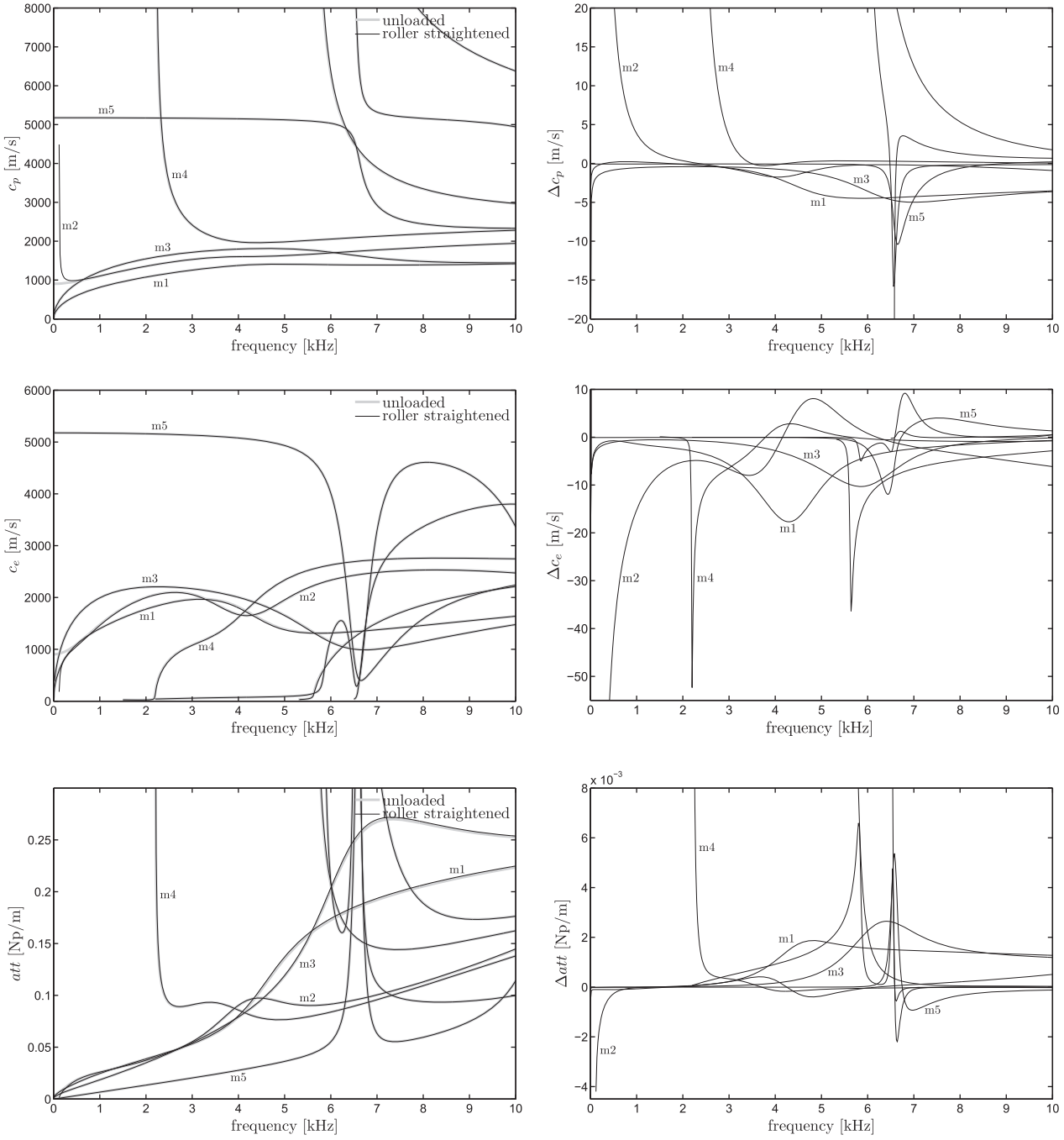

Fig. 6. Phase velocity, energy velocity and attenuation for the unloaded rail and the roller straightened rail in Keller et al. (2003).

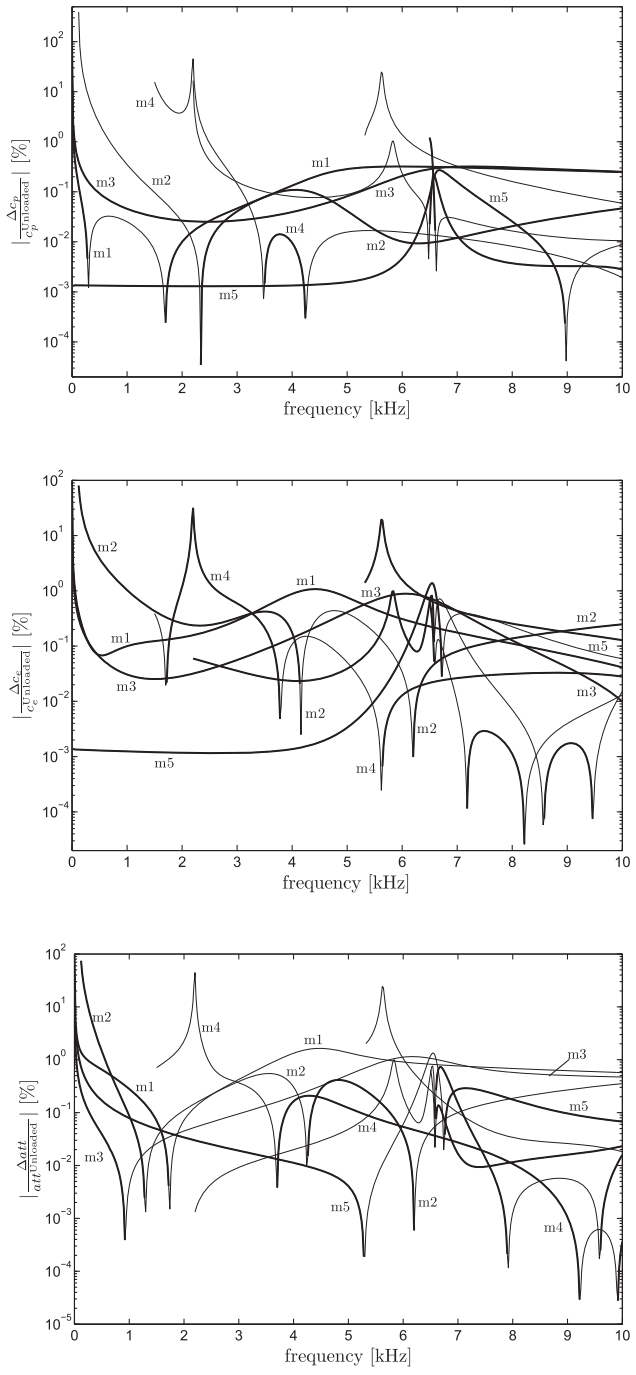

Fig. 7. Normalized phase velocity, energy velocity and attenuation variations between the loaded and unloaded cases for the viscoelastic roller straightened rail. Thin lines denote positive variations while thick lines denote negative variations.

on the left hand side of Fig. 3 show the phase velocity, energy velocity and attenuation dispersion curves for the elastic and viscoelastic rail without applied loads. It can be noted that the phase velocity and the energy velocity of the first five modes are almost unaffected by the presence of the material attenuation. The three graphs on the right hand side of Fig. 3 report the variations of the corresponding quantities due to the applied axial stress $\sigma^0_{zz} = 0,001\Re(E)$. The percent variations between the loaded and unloaded cases are shown in Fig. 4, with the thin lines denoting positive variations and the thick lines denoting negative variations. As it can be seen, the presence of an axial load leads to an increase in the phase velocity for the two flexural-like modes $m1$ and $m3$ at very low frequencies, which corresponds to a decrease of about 40 m/s in the energy velocity. It is interesting nothing that the maximum shift in the attenuation is located at about 4.5 kHz for the $m1$ mode and 6.2 kHz for the $m3$ mode. This trend is in contrast with that observed for the shift in phase and energy velocity of the two modes, which present their maximum for a frequency value approaching zero. Due to the decrease in attenuation, it follows that mode $m3$ at around 6 kHz could be a good candidate for revealing the state of σ^0_{zz} prestress in the waveguide.

The torsional-like mode $m2$ shows a positive Δc_p along the entire frequency range considered due to the tensile σ^0_{zz}. However, its energy velocity shows both positive and negative variations. The frequency values in correspondence of the maximum and minimum shift in the attenuation for the $m2$ mode are approximatively those with minimum and maximum shift on the energy velocity. Similar behavior can be observed also for the two flexural-like modes $m1$ and $m3$. Similarly to the previous modes, the flexural-like mode $m4$ presents an increase in the phase velocity for the entire frequency range, and an alternate trend for both energy velocity and attenuation. It can be noticed that while the flexural-like modes present their maximum shift in the phase velocity at very low frequency values (about 0 kHz for the $m1$ and $m3$ modes and in correspondence of the cutoff frequency for the $m4$ mode), the remaining two modes do not show this behavior. This is particularly evident for the $m5$ extensional-like mode, which presents its maximum at about 6.7 kHz. Moreover, at the same frequency value of about 6.5 kHz, the mode shows the maximum increase in the energy velocity and the maximum decrease in the attenuation with respect to the unloaded case. The maximum negative shift in the attenuation is not shown in the frequency-Δatt spectra of Fig. 3 for representative reasons, and its value is -0.016 Np/m.

4.2. Guided waves propagation in a new roll-straightened viscoelastic rail

Residual stresses in rails do not depend only on the loads occurring during the service life, but also on those arising from welding or manufacturing processes, which can be very large. A principal source of residual stresses is represented by the roller straightening, which is generally the last stage of the production cycle of the rail.

The residual stress formation in rails due to roller straightening has been intensively investigated in the last years (Schleinzer and Fischer, 2001; Keller et al., 2003; Biempica et al., 2009; Ringsberg and Lindbäck, 2003) and non destructive techniques, such as guided waves, can be very useful to determine the state of stress. To show the effect induced by the residual stress on the dispersive behavior in new roll-straightened rails, the stress patterns obtained by Keller et al. (2003) for the standard 113A profile have been considered. In particular, transversal, vertical and longitudinal contours of the residual stress are shown in Fig. 5 along with the finite element mesh.

The nonzero initial stress components $\sigma^0_{xx}, \sigma^0_{yy}$ and σ^0_{zz} are assumed to vary linearly over the generic finite element as a function of the stress value at each node, $\sigma^0_{ii}(\xi) = \sum_{j=1}^{3} N_j(\xi)\left(\sigma^0_{ii}\right)_j$, with the jth nodal stress value $\left(\sigma^0_{ii}\right)_j$ depending on the position of the node itself inside a specific stress region. The remaining stress components are neglected since of low order of magnitude.

The effect of the stress patterns on the guided waves dispersive characteristics is presented in Figs. 6 and 7 in the frequency range $0 \div 10$ kHz.

As previously noticed for the axially loaded rail, the dispersive behavior for the first five low order modes is only slightly influenced except for the $m2$ mode, which phase and energy velocity tend asymptotically to plus infinity and minus infinity for a

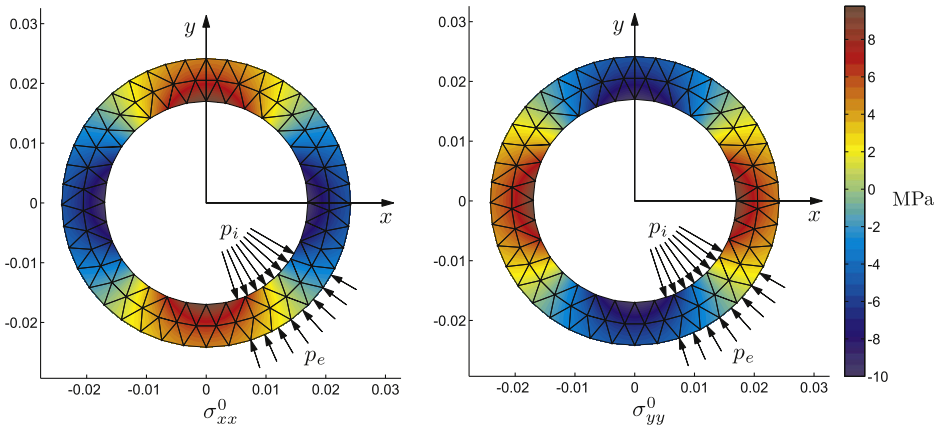

Fig. 8. Finite element mesh of 112 nodes and 150 linear triangular elements for the ASME 1-1/2 Schedule 160 pipe. The transversal stress contours are relative to an inner pressure $p_i = 10$ MPa and an outer pressure $p_e = 5$ MPa (case 3). Negative values denote compressive stresses.

frequency value tending to zero, respectively. At the same time, the mode attenuation decreases.

This particular behavior is not observed in the axially loaded rail and is a consequence of the presence of the transverse and vertical stresses σ^0_{xx} and σ^0_{yy}.

4.3. Pipe under initial pressure loading

In many practical situations the loads applied on the waveguide are dependent upon the deformation of the solid itself. This is the case, for instance, of a pressure acting at the inner and outer surfaces of a pipe when it undergoes to stress wave propagation, which is the case studied in this example.

The pressure fluctuations in the gas phase due to the solid–fluid interaction are neglected and the pressure is assumed to be constant during the motion. The pipe is considered sufficiently long to assume the cross-section in plain strain state in the prestressed configuration $\mathcal{C}$. For different inner and outer pressures p_i and p_e, the generic point (x_p, y_p) of the pipe cross section with center in $(x = 0,\ y = 0)$ is subjected to the following nonzero components of initial stress (see Fig. 8)

$$\sigma^0_{xx}, \sigma^0_{yy} = \left[\frac{c_1}{x_p^2+y_p^2} - c_2\right]\left(\frac{x_p^2, y_p^2}{x_p^2+y_p^2}\right) + \left[-\frac{c_1}{x_p^2+y_p^2} - c_2\right]\left(\frac{y_p^2, x_p^2}{x_p^2+y_p^2}\right)$$
$$\sigma^0_{zz} = \Re(\bar{\nu})\left(\sigma^0_x + \sigma^0_y\right) = -2\Re(\bar{\nu})\frac{p_e R_e^2 - p_i R_i^2}{R_e^2 - R_i^2} \tag{44}$$

where $\bar{\nu}$ is defined as in Eq. (42) and the constants c_1 and c_2 take the form

$$c_1 = \frac{R_i^2 R_e^2 (p_e - p_i)}{R_e^2 - R_i^2} \qquad c_2 = \frac{p_e^2 R_e^2 - p_i^2 R_i^2}{R_e^2 - R_i^2} \tag{45}$$

Positive values for the two pressures p_i and p_e produce compressive stresses σ^0_{xx} and σ^0_{yy}, which vary quadratically along the pipe wall thickness, while the axial stress σ^0_{zz} is constant for each point of the waveguide. The geometric stiffness matrices $\mathbf{k}^e_{\sigma^0_{xx}}$, $\mathbf{k}^e_{\sigma^0_{yy}}$ and $\mathbf{k}^e_{\sigma^0_{zz}}$ can be calculated by integrating via Gauss quadrature the stresses defined in Eq. (44) over each finite element. The numerical application considers an ASME 1-1/2 Schedule 160 steel pipe (outside radius $R_e = 24.15$ mm and inside radius $R_i = 17.01$ mm) subjected to a hydrostatic pressure gradient between the internal and the external surfaces.

The steel in the prestressed configuration is assumed as isotropic and hysteretic linear viscoelastic, having mass density $\rho = 7800$ kg/m^3, longitudinal and shear bulk waves equal to $c_L = 5963$ m/s and $c_S = 3187$ m/s respectively, longitudinal bulk wave attenuation $\kappa_L = 0.003$ Np/λ and shear bulk wave attenuation $\kappa_S = 0.008$ Np/λ.

The complex bulk velocities as well as the tensor of complex moduli are computed as in Eqs. (42) and (43). In Fig. 9 solutions relative to five cases are represented considering the mesh of 112 nodes and 150 linear triangular elements depicted in Fig. 8. In Fig. 10 the percent variations between the loaded and unloaded cases are shown. All the cases are studied by taking a reference pressure $p_{ref} = 5$ MPa. The continuous thick line denotes the stress free case (case 1), in which the pipe is not subjected to any pressure gradient. The solutions for the remaining four cases are obtained by varying the inner and outer pressures. In particular, the dashed line denotes an internal pressure $p_i = p_{ref}$ and $p_e = 0$ (case 2); the dotted line denotes that $p_i = 2p_{ref}$ and $p_e = p_{ref}$ (case 3); the dash dotted line refers to $p_i = 0$ and $p_e = p_{ref}$ (case 4), and finally, the continuous thin line indicates an internal pressure $p_i = p_{ref}$ and an external pressure $p_e = 2p_{ref}$ (case 5). As it can be seen in Fig. 9, the presence of a pressure gradient mostly affects the low order modes, essentially the torsional mode T(0,1) and the two flexural modes F(1,1). The most significant effect for this two modes is essentially related to changes in phase and energy velocities in the frequency range between 0 and 1000 Hz, which becomes larger if one assumes $p_{ref} > 5$ MPa.

The presence of an internal pressure only (case 2) produces a decrease of the phase velocity in the frequency range $0 \div 1000$ Hz for the torsional mode T(0,1), which become dispersive. At the same time, an increase of the phase velocity for the two flexural modes F(1,1) is observed in the frequency range $0 \div 50$ Hz, with a corresponding decrement in the energy velocity. This is principally due to the fact that an internal pressure produces a traction stress on the orthogonal direction z (see Eq. (45)), which translates into an additional geometric stiffness contribute and, as a consequence, into an increased flexural waves velocity (see also (Chen and Wilcox, 2007 and Loveday, 2009)). Moreover, an increase of the wave attenuation is observed for the torsional mode T (0,1) in the frequency range $0 \div 500$ Hz, while a further drop in the wave attenuation for the longitudinal mode L(0,1) is observed in the range $0 \div 100$ Hz (phase and energy velocities for this mode result to be substantially unchanged).

Dispersion curves for the cases 3, 4 and 5 show a similar behavior. In these cases the presence of an external pressure (lower than the internal pressure in the case 3 and higher in the cases 4 and 5) produces always a cutoff frequency and an increment in the phase velocity for the torsional mode T(0,1), which is limited to the

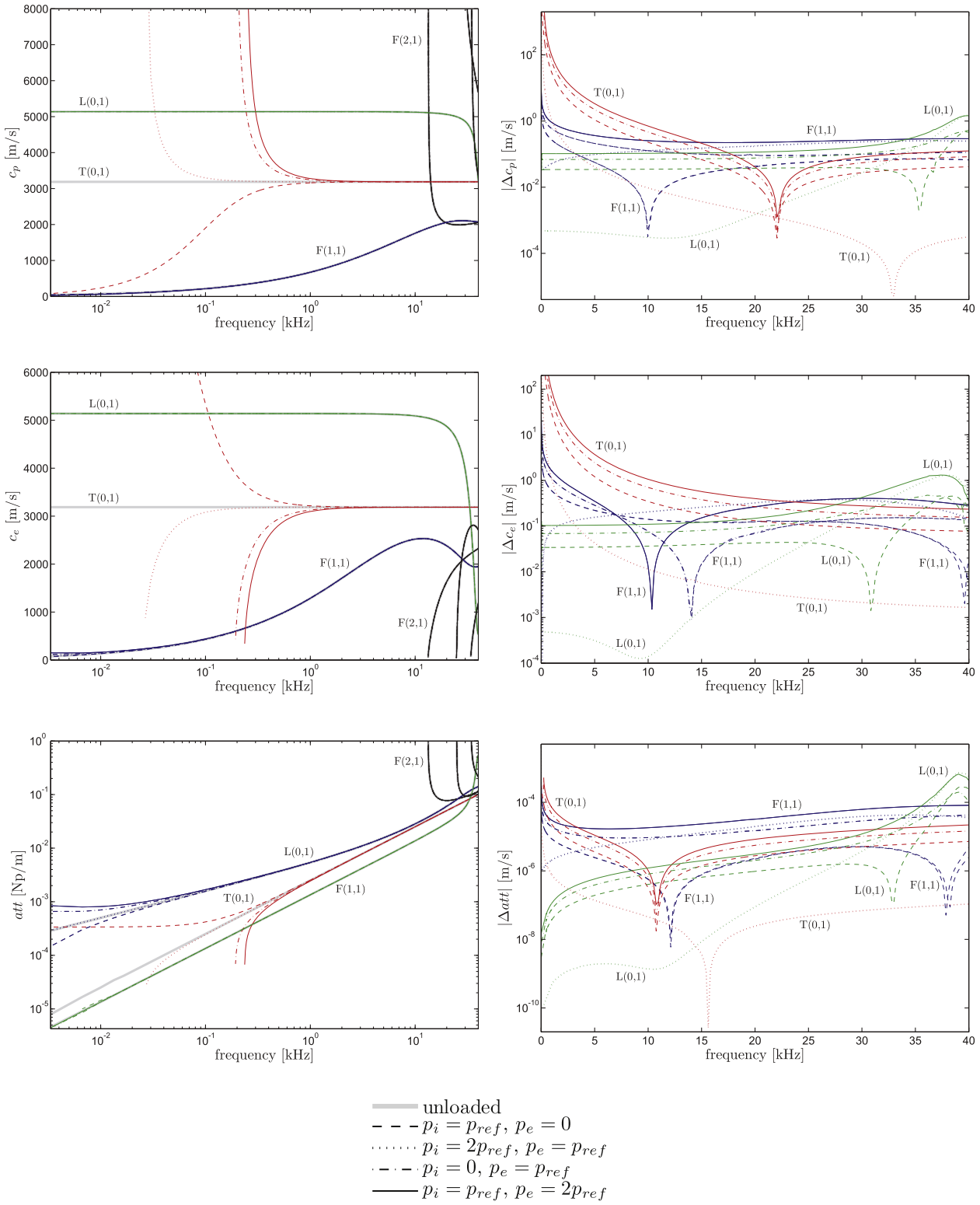

Fig. 9. Phase velocity, energy velocity and attenuation for the ASME 1-1/2 Schedule 160 pipe under different pressure gradients.

frequency range 25 ÷ 250 Hz for the case 3 and 190 ÷ 1500 Hz and 240 ÷ 1500 Hz for the cases 4 and 5, respectively. The related energy velocities are always increased for these cases.

In the same frequency ranges the wave attenuation of the T(0,1) mode is highly reduced by the presence of the prestress field and the phase velocity for the two flexural modes F(1,1) results to be lower than the stress-free case for each of the three cases considered. An interesting observation can be made about the behavior of the flexural mode F(1,1) in case 2 and case 3. In fact, even if in both cases the axial stress σ^0_{zz} is positive, in case 2 the effect of the internal pressure increases the mode phase velocity as a consequence of an increased geometric stiffness while in case 3 the extra external pressure reduces the mode phase velocity. As previously noticed for the case 2, only very small changes can be observed for the F(1,1) wave attenuation at very low frequencies, with a decrease on the attenuation values for the cases 3 and 4 and an

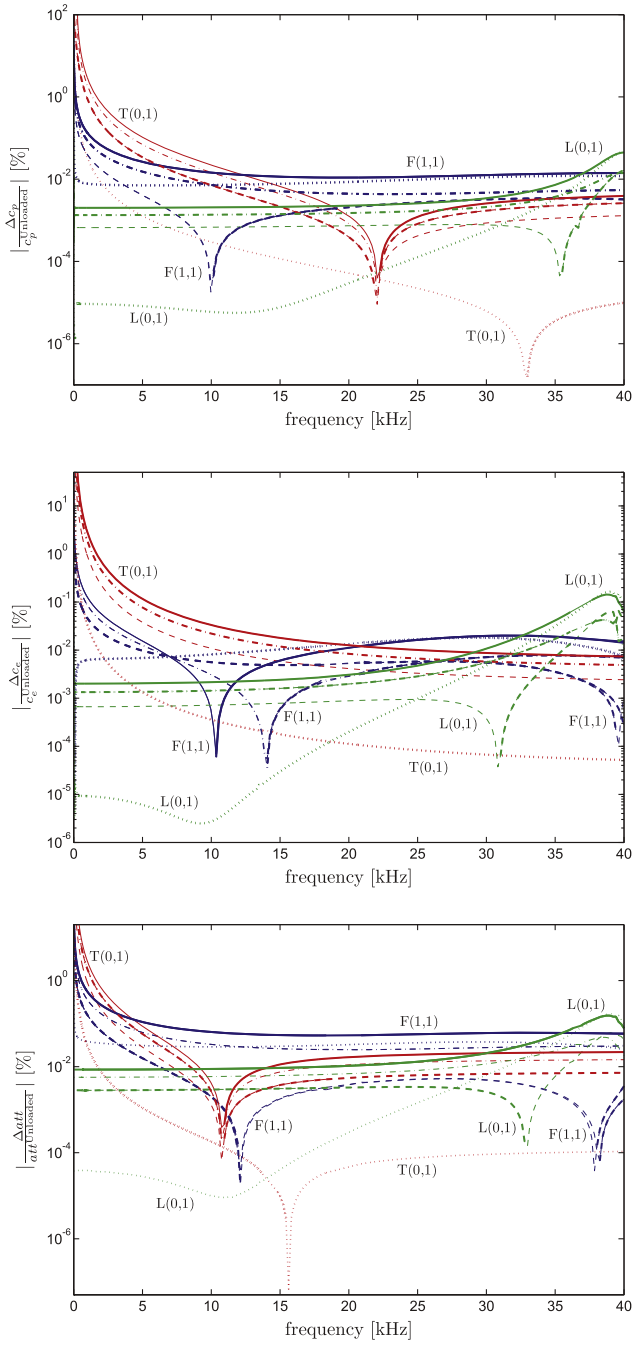

Fig. 10. Normalized phase velocity, energy velocity and attenuation variations between the loaded and unloaded cases for the viscoelastic pressurized pipe. Thin lines denote positive variations while thick lines denote negative variations.

increase for the case 5. However, an increment in the wave attenuation (very small for the case 3 and much higher for the cases 4 and 5) is observed for the longitudinal mode L(0,1) while its speed is not substantially affected by the presence of the pressure gradient.

5. Conclusions

An extension of the Semi Analytical Finite Element (SAFE) formulation has been presented to include the effect of a three dimensional prestress field in viscoelastic waveguides. Based on a semi-isoparametric discretization, the formulation of the problem has been extended by taking into account high order terms in the strain–displacement relations and complex elastic constants in the incremental stress–strain relations. The energy velocity formula has been also revisited to include initial stress terms starting from the balance law of the mechanical energy in material description. To show the capabilities of the method, some numerical investigation have been conducted on a 113A standard rail considering hysteretic material.

The rail has been analyzed in the $0 \div 10$ kHz frequency range, but knowledge of high-frequency dispersion data (up to 100 kHz) can be very helpful for axial load measurement.

For the case of an axial load only, the first flexural modes in the low frequency range are the most influenced, showing generally an increase in the phase velocity and a corresponding decrease in the energy velocity when a tensile load is applied. The phase and energy velocities of the first modes are mostly sensitive in the very low frequency range, although this does not happen for their corresponding wave attenuation, which show the highest changes in magnitude for higher frequency values.

In the case of a roller-straightened rail, the simultaneous presence of both longitudinal and transversal stresses modifies significantly the behavior of the fundamental torsional mode, while the sensitivity of the first flexural modes to the residual stress results to be highly mitigated with respect to the constant axial stress case. Although the analysis have been conducted in a low frequency range, the knowledge of high-frequency dispersion data (up to 100 kHz) can be very helpful for axial load measurement since some higher order modes remain considerable sensitive, providing useful informations in load detection schemes based on the measurement of the shift in phase produced by the load itself (Loveday and Wilcox, 2010).

The dispersive characteristic of guided waves propagating in a hysteretic ASME 1-1/2 Schedule 160 pipe have been also analyzed by considering the effect of a pressure gradient between the inner and outer surfaces. Similarly to the roller-straightened rail, the presence of the transversal (radial and circumferential) initial stresses affects principally the first torsional mode, which becomes dispersive, while the principal flexural mode is slightly influenced by the axial load which arise by considering the pipe in plane stress state.

Finally, it appears that the influence of the initial stress on the dispersive characteristics of compact sections is large for low order modes at low frequencies while higher order modes are generally less influenced. The reason is that at high frequencies the geometric stiffness contribution becomes very small if compared with the elastic stiffness contribution and therefore the wave propagation behavior mainly depends on the waveguide properties and it is slightly affected by the prestress state (Chen and Wilcox, 2007).

Based on the proposed numerical examples, the frequency values corresponding to the highest shift in the attenuation for the principal modes seem generally far to those at which the highest shift in the phase and energy velocity are observed. This particular behavior could be deepened by assuming a different viscoelastic model as, for example, the Kelvin–Voigt model or the Linear Standard Solid.

The obtained results can be helpful to design testing conditions in guided waves based inspection of rails and pressurized pipelines.

Acknowledgements

This topic is one of the research thrusts of the Centre of Study and Research for the Identification of Materials and Structures (CIMEST) of the University of Bologna (Italy).

References

Achenbach, J.D., 1973. Wave Propagation in Elastic Solids. North-Holland Pub. Co., Amsterdam.

Bartoli, I., Coccia, S., Phillips, R., Srivastava, A., di Scalea, F.L., Salamone, S., 2010. Stress dependence of guided waves in rails. In: Kundu, T. (Ed.), Health Monitoring of Structural and Biological Systems 2010, Proc. SPIE, vol. 7650, pp. 765021-1–765021-10.

Bartoli, I., Marzani, A., Lanza di Scalea, F., Viola, E., 2006. Modeling wave propagation in damped waveguides of arbitrary cross-section. Journal of Sound and Vibration 295, 685–707.

Bathe, K.-J., 1996. Finite Element Procedures. Prentice Hall, Upper Saddle River, New Jersey, p. 07458.

Bažant, Z.P., Cedolin, L., 1991. Stability of Structures: Elastic, Inelastic, Fracture and Damage Theories. Oxford University Press, New York.

Bhaskar, A., 2003. Waveguide modes in elastic rods. Proceedings: Mathematical, Physical and Engineering Sciences 459 (2029), 175–194.

Biempica, C.B., del Coz Dí-az, J., Nieto, P.G., Sánchez, I.P., 2009. Nonlinear analysis of residual stresses in a rail manufacturing process by fem. Applied Mathematical Modelling 33 (1), 34–53.

Biot, M.A., 1940. The influence of initial stress on elastic waves. Journal of Applied Physics 11 (8), 522–530.

Biot, M.A., 1957. General theorems on the equivalence of group velocity and energy transport. Physical Review 105 (4), 1129–1137.

Biot, M.A., 1965. Mechanics of Incremental Deformations. John Wiley & Sons Inc., New York.

Bonet, J., Wood, R.D., 2008. Nonlinear Continuum Mechanics for Finite Element Analysis. Cambridge University Press, New York.

Brillouin, L., 1960. Wave Propagation and Group Velocity. Academic Press, New York.

Caviglia, G., Morro, A., 1992. Inhomogeneous Waves in Solids and Fluids. World Scientific Publishing Co. Pte. Ltd., Farrer Road, Singapore.

Caviglia, G., Morro, A., 1998. Energy flux and dissipation in pre-stressed solids. Acta Mechanica 128, 209–216.

Chaki, S., Bourse, G., 2009. Guided ultrasonic waves for non-destructive monitoring of the stress levels in prestressed steel strands. Ultrasonics 49 (2), 162–171.

Chang, Y., Ho, B., 1995. The poynting theorem of acoustic wave propagating in an inhomogeneous moving medium. Journal of Sound and Vibration 184 (5), 942–945.

Chen, F., Wilcox, P.D., 2007. The effect of load on guided wave propagation. Ultrasonics 47 (1–4), 111–122.

Christensen, R.M., 2010. Theory of Viscoelasticity: Second Edition. Dover Publications, Inc., Mineola, NY.

Cook, L.P., Holmes, M., 1981. Waves and dispersion relations for hydroelastic systems. SIAM Journal on Applied Mathematics 41 (2), 271–287.

Davidovich, M., 2010. On the electromagnetic energy density and energy transfer rate in a medium with dispersion due to conduction. Technical Physics 55, 630–635.

Degtyar, A.D., Rokhlin, S.I., 1998. Stress effect on boundary conditions and elastic wave propagation through an interface between anisotropic media. Journal of Acoustical Society of America 104 (4), 1992–2003.

Frikha, A., Treyssède, F., Cartraud, P., 2011. Effect of axial load on the propagation of elastic waves in helical beams. Wave Motion 48 (1), 83–92.

Gerasik, V., Stastna, M., 2010. Complex group velocity and energy transport in absorbing media. Physical Review E 81, 056602.

Hayes, M., 1963. Wave propagation and uniqueness in prestressed elastic solids. Proceedings of the Royal Society of London. Series A, Mathematical and Physical Sciences 274 (1359), 500–506.

Holzapfel, G.A., 2000. Nonlinear Solid Mechanics. John Wiley & Sons Ltd, Baffins Lane, Chichester.

Keller, J., Prime, M.B., Buttle, D., Mummery, P.M., Webster, P.J., Shackleton, J., Withers, P.J., 2003. The measurement of residual stress in railway rails by diffraction and other methods. Journal of Neutron Research 11 (4), 187–193.

Lee, U., Oh, H., 2005. Dynamics of an axially moving viscoelastic beam subject to axial tension. International Journal of Solids and Structures 42 (8), 2381–2398.

Lematre, M., Feuillard, G., Clézio, E.L., Lethiecq, M., 2006. Modeling of the influence of a prestress gradient on guided wave propagation in piezoelectric structures. Journal of Acoustical Society of America 120, 1964–1975.

Lighthill, M.J., 1965. Group velocity. Journal of the Institute of Mathematics and its Applications 1, 1–28.

Loveday, P.W., 2009. Semi-analytical finite element analysis of elastic waveguides subjected to axial loads. Ultrasonics 49 (3), 298–300.

Loveday, P.W., Wilcox, P.D., 2010. Guided wave propagation as a measure of axial loads in rails. In: Kundu, T. (Ed.), Health Monitoring of Structural and Biological Systems 2010, Proc. SPIE, vol. 7650, pp. 765023-1–765023-8.

Man, C.-S., 1998. Hartig's law and linear elasticity with initial stress. Inverse Problems 14 (2), 313–319.

Mu, J., Rose, J.L., 2008. Guided wave propagation and mode differentiation in hollow cylinders with viscoelastic coatings. Journal Acoustical Society of America 124, 866–874.

Osetrov, A.V., Fröhlich, H.-J., Koch, R., Chilla, E., 2000. Acoustoelastic effect in anisotropic layered structures. Physical Review B 62, 13963–13969.

Ringsberg, J.W., Lindbäck, T., 2003. Rolling contact fatigue analysis of rails including numerical simulations of the rail manufacturing process and repeated wheel-rail contact loads. International Journal of Fatigue 25 (6), 547–558.

Rose, J.L., 2004. Ultrasonic Waves in Solid Media. Cambridge University Press, Cambridge.

Schleinzer, G., Fischer, F., 2001. Residual stress formation during the roller straightening of railway rails. International Journal of Mechanical Sciences 43 (10), 2281–2295.

Shen, L.-H., Wang, Y.-M., Sun, F.-R., 2008. Study on feasibility of pressure pipe guided wave ndt based on magnetostrictive effect. In: Ultrasonics Symposium 2008. IUS 2008. IEEE, pp. 1897–1900.

Shin, H.J., Rose, J.L., 1999. Guided waves by axisymmetric and non-axisymmetric surface loading on hollow cylinders. Ultrasonics 37 (5), 355–363.

Tanuma, K., Man, C.-S., 2006. Perturbation formula for phase velocity of Rayleigh waves in prestressed anisotropic media. Journal of Elasticity 85, 21–37.

Treyssède, F., 2008. Elastic waves in helical waveguides. Wave Motion 45 (4), 457–470.

Whitam, G., 1974. Linear and Nonlinear Waves. Wiley, New York.

Williams, R.A., Malvern, L.E., 1969. Harmonic dispersion analysis of incremental waves in uniaxially prestressed plastic and viscoplastic bars, plates, and unbounded media. Journal of Applied Mechanics 36 (1), 59–64.

Wriggers, P., 2008. Nonlinear Finite Element Methods. Springer-Verlag, Berlin, Heidelberg.

Yang, Y.-B., Kuo, S.-R., 1994. Nonlinear Framed Structures. Prentice Hall, New York.